remote sensing

MDPI

Review

Water Ice Resources on the Shallow Subsurface of Mars: Indications to Rover-Mounted Radar Observation

Naihuan Zheng [1], Chunyu Ding [1,2,*], Yan Su [3,4] and Roberto Orosei [5]

[1] Institute for Advanced Study, Shenzhen University, Shenzhen 518060, China; 2020281080@email.szu.edu.cn
[2] Tiandu-Shenzhen University Deep Space Exploration Joint Laboratory, Shenzhen 518060, China
[3] Key Laboratory of Lunar and Deep Space Exploration, National Astronomical Observatories, Chinese Academy of Sciences, Beijing 100049, China; suyan@nao.cas.cn
[4] School of Astronomy and Space Science, University of Chinese Academy of Sciences, Beijing 100049, China
[5] Istituto di Radioastronomia, Istituto Nazionale di Astrofisica, Via Piero Gobetti 101, 40129 Bologna, Italy; roberto.orosei@inaf.it
* Correspondence: dingchunyu@szu.edu.cn

Abstract: The planet Mars is the most probable among the terrestrial planets in our solar system to support human settlement or colonization in the future. The detection of water ice or liquid water on the shallow subsurface of Mars is a crucial scientific objective for both the Chinese Tianwen-1 and United States Mars 2020 missions, which were launched in 2020. Both missions were equipped with Rover-mounted ground-penetrating radar (GPR) instruments, specifically the RoPeR on the Zhurong rover and the RIMFAX radar on the Perseverance rover. The in situ radar provides unprecedented opportunities to study the distribution of shallow subsurface water ice on Mars with its unique penetrating capability. The presence of water ice on the shallow surface layers of Mars is one of the most significant indicators of habitability on the extraterrestrial planet. A considerable amount of evidence pointing to the existence of water ice on Mars has been gathered by previous researchers through remote sensing photography, radar, measurements by gamma ray spectroscopy and neutron spectrometers, soil analysis, etc. This paper aims to review the various approaches utilized in detecting shallow subsurface water ice on Mars to date and to sort out the past and current evidence for its presence. This paper also provides a comprehensive overview of the possible clues of shallow subsurface water ice in the landing area of the Perseverance rover, serving as a reference for the RIMFAX radar to detect water ice on Mars in the future. Finally, this paper proposes the future emphasis and direction of rover-mounted radar for water ice exploration on the Martian shallow subsurface.

Keywords: Mars; water ice; shallow subsurface; Martian-based ground-penetrating radars; RoPeR radar; RIMFAX radar

Citation: Zheng, N.; Ding, C.; Su, Y.; Orosei, R. Water Ice Resources on the Shallow Subsurface of Mars: Indications to Rover-Mounted Radar Observation. *Remote Sens.* **2024**, *16*, 824. https://doi.org/10.3390/rs16050824

Academic Editor: Lorenzo Capineri

Received: 7 January 2024
Revised: 23 February 2024
Accepted: 23 February 2024
Published: 27 February 2024

1. Introduction

The search for extraterrestrial water resources has been a key scientific objective in the human exploration of the solar system, with Mars being the second closest terrestrial planet and the most likely candidate to have water resources. Scientists have been exploring Mars with space probes since 1960 (Masursky [1], Zheng [2], Li et al. [3]), and after more than sixty years of exploration, the red planet is slowly revealing its secrets to mankind.

In 2002, the Mars Odyssey spacecraft discovered possible frozen water on the surface layer of Mars (Boynton et al. [4]). Back in the 1960s, it was thought that the two polar caps consisted mainly of frozen carbon dioxide and a small amount of water ice (McDougal et al. [5]). In the late 1970s, it was shown that there was water ice underneath the carbon dioxide ice covering of the north polar cap according to the observation of the Viking orbiters. However, experts continued to believe that the southern polar cap was made of

carbon dioxide ice (Kieffer [6]). In 2003, Byrne and Ingersoll [7] argued, based on high-resolution images from Mars Global Surveyor and thermal images from Mars Odyssey, that the Martian polar ice caps are made almost entirely of water ice, with only a thin layer of carbon dioxide ice on its surface. This was confirmed through direct spectroscopic observations by Bibring et al. [8]. In 2008, the Phoenix mission confirmed water existed on Mars by identifying water vapor when heating Martian soil samples (Rennó et al. [9]). Remote sensing data suggest that Mars once had large oceans and lakes (Clifford and Parker [10], McEwen et al. [11], Michalski et al. [12]). Moreover, recurring slope lineae suggest there may be seasonal flowing liquid water on Mars (McEwen et al. [13]). The presence of water ice on the surface of Mars can also be inferred by measuring the concentration of hydrogen on the shallow subsurface of Mars through neutron detectors and calculating the abundance of hydrogen. However, these observations are not penetrating and only reflect the physical properties of very thin areas of the Martian surface. The Martian-based ground-penetrating radar is a unique way to explore the presence of water ice on the shallow surface layer of Mars within a few meters to tens of meters (Hamran et al. [14], Zhou et al. [15], Chen et al. [16], Zhang et al. [17]).

Martian orbiter-based radars are mainly focused on the observation of water ice over the entirety of Mars, which includes the Mars Advanced Radar for Subsurface and Ionosphere Sounding (MARSIS) on the Mars Express spacecraft, Shallow Radar (SHARAD) on the Mars Reconnaissance Orbiter (MRO) and The Mars orbiter subsurface investigation radar (MOSIR) on China's Tianwen-1 mission (Picardi et al. [18,19]). But orbiter-based radars are not sensitive to the detection of water ice at depths of several meters due to their limited vertical resolution (Li et al. [3], Seu et al. [20,21], Hong et al. [22,23], Qiu and Ding [24]). In 2020, China and the United States launched the Tianwen-1 and Mars 2020 missions, respectively. China's Tianwen-1 mission landed on the Utopian Planitia (109°55′30″E, 25°3′58″N) (Li et al. [3]), and the Perseverance rover landed on the Jezero crater (77°27′3″E, 18°26′4″N) (Hamran et al. [25]). These missions carry advanced detection instruments, such as in situ spectrometers and highly accurate ground-penetrating radars. The Rover-mounted Subsurface Penetrating Radar (RoPeR) is onboard the Zhurong Rover (Zhou et al. [15], Chen et al. [16], Li et al. [26]), while the Radar Imager for Mars' Subsurface Experiment (RIMFAX) is onboard the Perseverance rover (Hamran et al. [14], Casademont et al. [27]). Both of the Martian-based ground-penetrating radars can detect water ice within a few meters or tens of meters of the shallow surface of Mars (Hamran et al. [14], Zhou et al. [15]). In addition, the European Space Agency (ESA) plans to launch the Exomars Mars exploration mission in 2028, which also will carry WISDOM (the Water Ice Subsurface Deposit Observation on Mars), a ground penetrating radar, onboard the rover (Herve et al. [28]). These Martian-based ground-penetrating radars will be used primarily to reveal the geologic framework of the subsurface layers of Mars and the evolutionary history of its surface processes, and to detect water ice, or even liquid water, on the shallow subsurface of Mars.

This paper reviews the evidence for water ice on Mars obtained from previous studies using various observations, which are discussed in Section 2, including remote sensing photography (see Section 2.1), radar observation (see Section 2.2), measurements by gamma-ray spectroscopy and neutron spectrometers (see Section 2.3), soil analysis (see Section 2.4), and other observation methods (see Section 2.5); Section 3 reviews the evidence of water ice on the shallow surface layers of Mars in the old days, including canyon network features (see Section 3.1), paleolake features (see Section 3.2), marine remains (see Section 3.3), rampart craters and polygonal terrain (see Section 3.4), and other surface geological features (see Section 3.5); Section 4 provides an overview of the current evidence of water ice in the shallow subsurface of Mars, including results from in situ spectroscopic observation (see Section 4.1) and radar detection (see Section 4.2); Section 5 summarizes the findings derived from the ground-penetrating radar in the landing area of the Perseverance rover; Section 6 discusses the limitations and breakthroughs in ground-penetrating radar to detect water ice on the Martian shallow subsurface. Finally, the advantages and development

trends of in situ ground-penetrating radar for detecting water ice in the shallow surface layer of Mars are presented (see Section 7). Assessing the feasibility of human colonization on Mars greatly depends on comprehending the spatial distribution of water ice and liquid water within the shallow subsurface layer of Mars, alongside the evolutionary patterns of water ice resources.

2. Detection Techniques of Shallow Surface Water Ice

Since 1961, more than forty Mars exploration missions have been conducted by humans. The detection of water ice in the shallow surface layers of Mars has long been a primary objective of these missions, as it is a crucial factor in the search for signs of life on the planet Mars. A comprehensive review of the successful missions reveals that the historical detection of water ice in the shallow surface layers of Mars can be categorized into several methods, including remote-sensing photography, radar, gamma-ray spectroscopy, neutron spectrometers, soil analysis, and other ancillary analyses.

2.1. Remote Sensing Photography

Remote sensing photography utilizes high-resolution imaging cameras onboard orbiters or rovers to capture images of the surface of Mars. This method enables direct observation of the presence or absence of landforms formed by liquid water on the planet's surface. Several typical Mars imaging cameras include the Mars Orbiting Camera (MOC) carried by the Mars Global Surveyor (MGS), which can capture images with high resolution, e.g., the captured images have a resolution of 1.5–12 m/pixel (Malin et al. [29]). MRO is equipped with several cameras, e.g., the Mars Color Imager (MARCI), the High-Resolution Imaging Science Equipment (HiRISE), and the Context Camera (CTX). The SuperCam onboard the Perseverance rover is equipped with the remote micro-imager (RMI); the RMI can distinguish the grains as small as 160 μm at a distance of 2 m from the instrument with a resolution $\leq$ 80 μrad (Wiens et al. [30]). The Colour and Stereo Surface Imaging System (CaSSIS) onboard ESA's Exomars Trace Gas Orbiter (TGO) can acquire surface images at a resolution of ~4.6 m/pixel, including stereo imaging and color information (Thomas et al. [31]).

Extensive remote sensing photography has enabled the acquisition of imagery of the Martian surface, such as Figure 1a, which depicts the Acidalia mesas captured by HiRISE. The interpretation of this image suggests similarities to the Tuya landscape on Earth, indicating the possible existence of volcano–ice interaction terrain on Mars (Martínez-Alonso et al. [32]). This observation provides evidence that the mysterious landforms on Mars have been influenced by water and ice (Martínez-Alonso et al. [32]). The Galaxias Fossae region photographed by CTX (Figure 1b) is interpreted as exhibiting possible ice-fall-like and ice-flow morphologies (Pedersen et al. [33]). Furthermore, by comparison of recurring slope lineae (RSL) images captured by HiRISE with surface temperature and water vapor images at the same time at Martian solar longitude (Ls) 142.7° and Ls 348.7° (Figure 2), the temperature increases from 158 K to 261 K, while the water vapor increases from 0.0013 kg/m^2 to 0.0097 kg/m^2. It reinforces the possibility that the triggering mechanism of RSL requires sufficient water and temperature (Howari et al. [34]). Additionally, the orbiter of the Chinese Tianwen-1 mission is equipped with medium- and high-resolution cameras (0.5 m@265 km) for imaging of key areas where water may be present (Li et al. [3]).

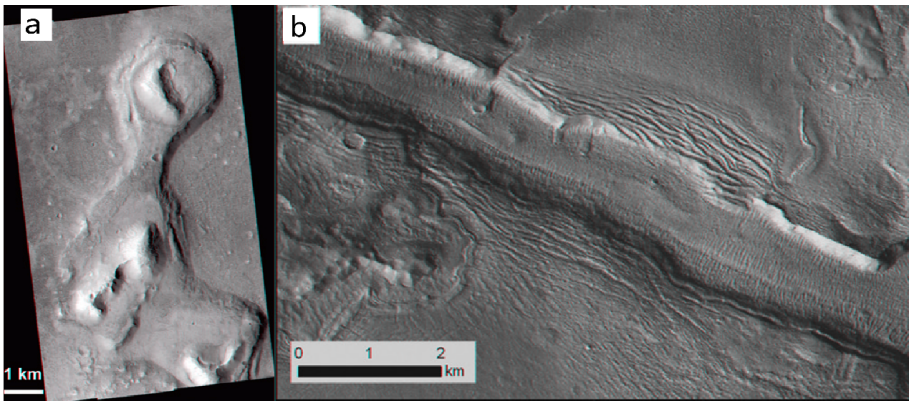

Figure 1. (**a**) The Acidalia mesas are considered to be flat-topped mountains (adapted from Martínez-Alonso et al. [32]); (**b**) an example from Galaxias Fossae (adapted from Pedersen and Head [35]).

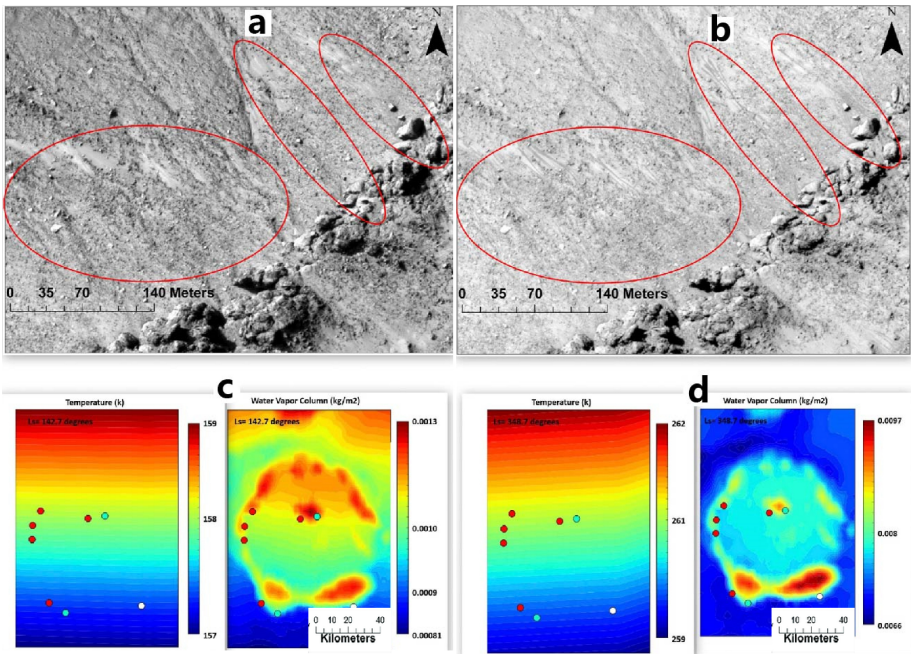

Figure 2. (**a**,**b**) display HiRISE data for Asimov crater (47°S, 5°E) at Ls 142.7° and Ls 348.7°, respectively, showcasing variations in recurring slope lineae (red circles) in the images. (**c**,**d**) depict relevant atmospheric parameters that were captured at the same time as the HiRISE data acquisition on the Martian surface (adapted from Howari et al. [34]).

2.2. Radar Observation

The detection of shallow surface water ice on Mars is primarily accomplished through the use of radar equipment on orbiters or Mars rovers (Zhou et al. [15], Picardi et al. [18,19], Seu et al. [20,21], Zhou et al. [36]). The working principle of the Martian-based ground-penetrating radar can be summarized as follows (Zhou et al. [15], Qiu and Ding [24]): The radar antenna emits radar pulses towards the subsurface of Mars. When the radar electromagnetic waves encounter differences in impedance from subsurface materials, reflections and scattering of the electromagnetic waves occur at the interfaces between different materials. These echo signals are then captured by the radar antenna. The data received by the radar are then analyzed to calculate the subsurface stratification and thickness of the soil on Mars (Chen et al. [16]), as well as the dielectric properties of the subsurface material, such as the value of dielectric loss and relative permittivity. By determining the polarization of the radar signal, it is potentially feasible to ascertain the presence of water ice in the superficial layers of the detection area (Zhou et al. [36], Dong et al. [37], Liu et al. [38]). By processing these echo

signals, the subsurface structure of Mars' surface and the composition of the subsurface materials can also be revealed (Grima et al. [39], Nouvel et al. [40]).

Orbiter-based radars such as MARSIS, SHARAD, and MOSIR are used to detect the global scale of Mars, with the advantage of a wide detection range. In situ ground-penetrating radars, such as RoPeR and the RIMFAX, are used for localized detection in the landing areas and have the advantage of higher precision to examine the localized subsurface structure with an unprecedented resolution compared to those of orbiter-based ground-penetrating radar.

Installed on the ESA's Mars Express space probe, the Mars Advanced Radar for Subsurface and Ionosphere Sounding (MARSIS) operates at central frequencies of 1.8, 3, 4, and 5 MHz (Picardi et al. [18,19]). With a theoretical penetration depth of 0.5–5 km, the radar is primarily used to detect the distribution of water ice beneath the Martian subsurface, local geological stratigraphy, and subsurface aquifers (Jordan et al. [41]).

Similarly, the Mars Reconnaissance Orbiter (MRO) carries shallow radar (SHARAD) with a central frequency of 20 MHz and a theoretical penetration depth of 0.1–1 km (Seu et al. [21]). SHARAD is capable of detecting stratified structures up to one kilometer below the Martian surface and is primarily used for detecting water ice, geological subsurface structure, and subsurface aquifers below the subsurface of Mars (Seu et al. [20], Xiong et al. [42]).

For instance, Bramson et al. [43] compared the time delay between surface and subsurface radar reflector from SHARAD (Figure 3c) with the terrace depth (Figure 3b) of terrace-type crater within the Arcadia Planitia determined by digital terrain models (DTMs) from HiRISE (Figure 3a), to work out the dielectric constant and constrain the materials' composition, and finally suggested that much of the upper region of the area is likely to be water ice. Anomalously bright subsurface reflections were identified in MARSIS radar observations collected from May 2012 to December 2015 over Planum Australe (Figure 4), which were construed as due to the presence of liquid water at the bottom of the SPLDs (Orosei et al. [44]).

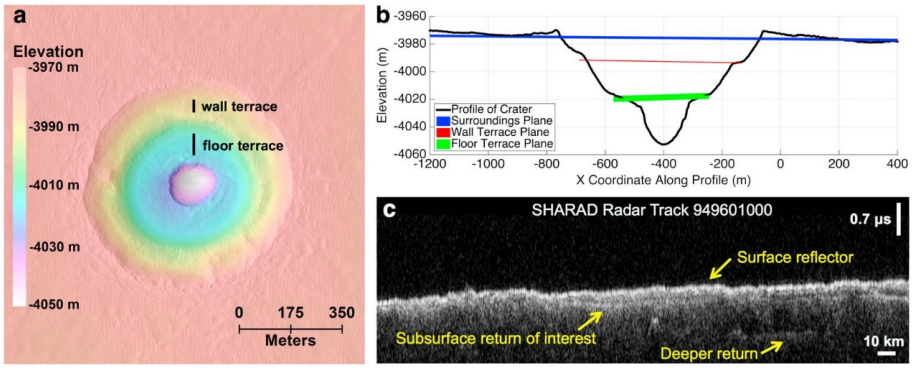

Figure 3. (**a**) DTM of the double terrace crater. (**b**) Crater profile with planes close to the surroundings and the elevation of each terrace. (**c**) SHARAD radar observations through Badger Crater. (Adapted from Bramson et al. [43]).

China's Tianwen-1 spacecraft with MOSIR subsurface detection radar is currently exploring Mars, but the relevant detection data and research results have not yet been officially released (Li et al. [3], Fan et al. [45]). Its high-frequency mode operates at a center frequency ranging from 30 to 50 MHz, while its low-frequency mode operates at a center frequency of 10–15 MHz and 15–20 MHz (Fan et al. [45]). It has a subsurface structure penetration depth of about 100 m and an ice penetration depth of about 1000 m (Fan et al. [45]). Its thickness resolution capability is at the meter level, and it is primarily utilized for detecting water ice and subsurface structure on Mars (Li et al. [3], Hong et al. [22], Fan et al. [45]).

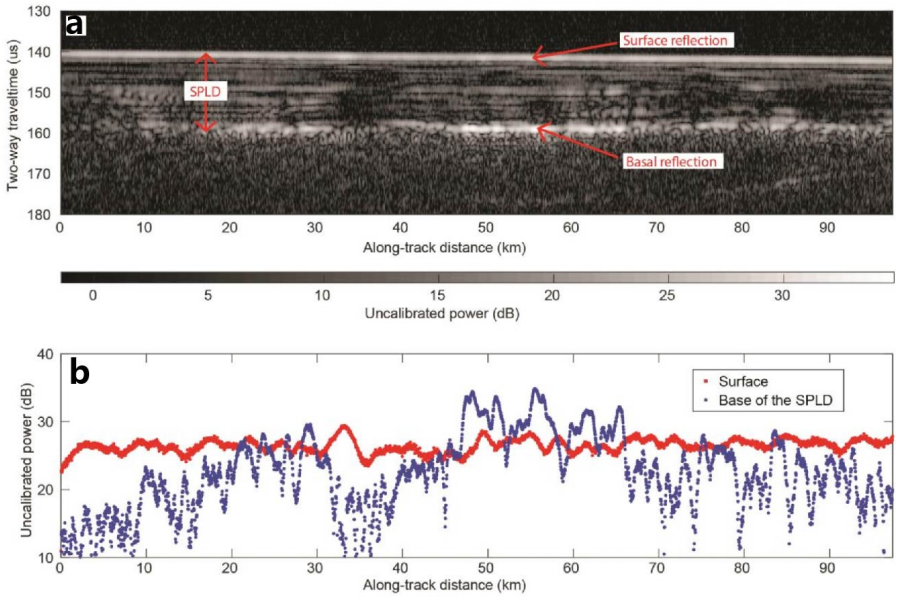

Figure 4. Radar data collected by MARSIS radar for the Planum Australe region on the southern pole of Mars. (**a**) Radargram for MARSIS orbit 10737. the bottom reflector corresponds to the South Polar Layered Deposits (SPLDs)/basal material interface. (**b**) Plot of surface and basal echo power for the radargram in (a) (adapted from Orosei et al. [44]).

Martian-based ground-penetrating radars are also beginning to be deployed on the surface of Mars to reveal the secrets beneath its surface (Hamran et al. [25], Li et al. [26]). For instance, the Zhurong rover carries an in situ detection radar, RoPeR, which is a Martian-based ground-penetrating radar (Zhou et al. [15]). It operates at 15–95 MHz for the low-frequency channel and 450–2150 MHz for the high-frequency channel (Table 1), with thickness resolution at the meter and centimeter levels, respectively. It can be used to detect the regions with depths of tens of meters below the Martian surface (Zhou et al. [15], Chen et al. [16], Li et al. [26]). The Perseverance rover also carries a Martian-based ground-penetrating radar, RIMFAX, primarily used to detect shallow surface geological structures and water ice on Mars [46]. Additionally, the ESA plans to carry a Martian-based ground-penetrating radar named WISDOM on board the ExoMars Rover soon (Herve et al. [28]).

Table 1. The carried ground-penetrating radars and their basic parameters both in Mars and lunar exploration missions.

Mission	GPR Name	Center Frequency	Frequency Band	Depth Resolution	Penetration Depth	References
China's Zhurong Rover	RoPeR	55 MHz	15–95 MHz	A few meters	10–100 m	Zhou et al. [15]
		1300 MHz	450–2150 MHz	A few centimeters	3–10 m	Zhou et al. [15]
Perseverance Rover	RIMFAX	675 MHz	150–1200 MHz	10–40 cm	>10 m	Hamran et al. [14]
ExoMars	WISDOM	1750 MHz	500–3000 MHz	≈3 cm	3–10 m	Ciarletti et al. [47]
Chang'e-3/-4	LPR	60 MHz	40–80 MHz	meter-scale	>100 m	Fang et al. [48]
	LPR	500 MHz	250–750 MHz	≤30 cm	>30 m	Fang et al. [48]
Chang'e-5	LRPR	2000 MHz	1000–3000 MHz	≈5 cm	>3 m	Xiao et al. [49]

2.3. Measurements by Gamma Ray Spectroscopy and Neutron Spectrometers

The Gamma Ray Spectrometer (GRS) onboard NASA's Mars Odyssey allows for the mapping of the chemical makeup on Mars to depths of 10 cm to 1 m below the surface through the measurement of gamma rays from space and their interactions with various surface materials (Evans et al. [50], Saunders et al. [51]). The GRS consists of the

Gamma Sensor (GS), the Neutron Spectrometer (NS), and the High-Energy Neutron Detector (HEND). The neutron detector equipment like NS and HEND measures neutrons with different energy levels liberated from the near-surface of Mars by cosmic rays. It analyzes the energy reaction between neutrons and hydrogen nuclei and measures the gamma rays to obtain the content of hydrogen atoms (water and potential organic matter) in the soil at different depths, thus inferring water ice does exist on the near-surface (Saunders et al. [51]). This enables the identification of the number and type of chemical elements present, as well as the distribution of hydrogen, which can provide evidence of water ice (Evans et al. [50], Saunders et al. [51]). The GRS is capable of planet-wide mapping of hydrogen abundance on Mars at a spatial resolution of approximately 600 km, enabling inferences to be made that water ice may exist near the Martian surface (Saunders et al. [51]).

Boynton et al. [4] utilized the GRS observation to create a superthermal neutron flux map from the neutron energy spectrometer (Figure 5). Through this analysis, two hydrogen-rich regions near the Martian northern pole and southern pole were identified, suggesting that the source of this hydrogen in the subsurface may be ice. The globally distributed superthermal neutron flux map can be used to assist in the interpretation of whether Martian-based ground-penetrating radar detects regions of water ice.

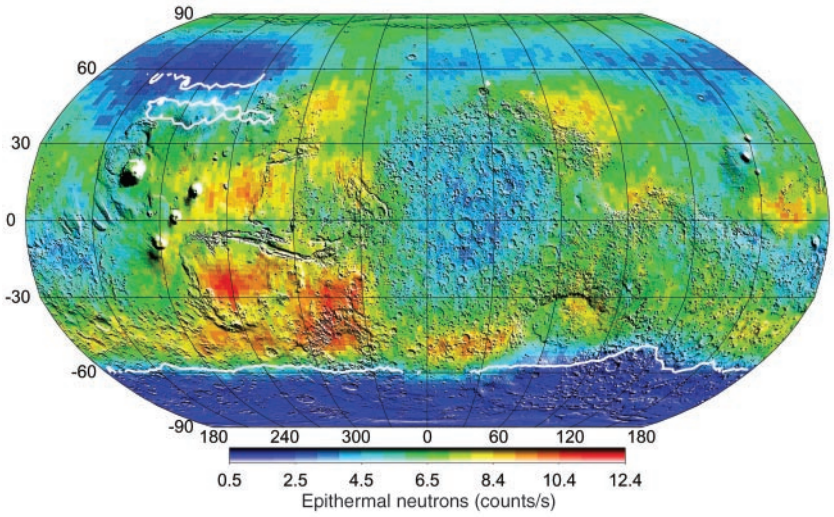

Figure 5. Super thermal neutron flux map created using data from the neutron energy spectrometer (adapted from Boynton et al. [4]).

The distribution of superthermal neutrons for 55 days at energies ranging from 0.4 eV to 100 keV plotted by HEND (Figure 6) suggested that the deviation of the mean and maximum neutron count rates in the northern and southern hemispheres corresponds to 5% water by weight in the homogeneous subsurface layer, with the higher content likely related to chemically bound water in the subsurface layer. The low superthermal neutron flux in the south is due to the higher water ice content within the lower subsurface layer than the upper subsurface. Under this hypothesis, Mars has large areas at low-elevation regions of the northern hemisphere and high-elevation regions of the southern hemisphere that contain the uppermost subsurface hydrogen, which may be bound in water ice. This hypothesis requires support from the global surface and subsurface water transport mechanisms on Mars (Mitrofanov et al. [52]).

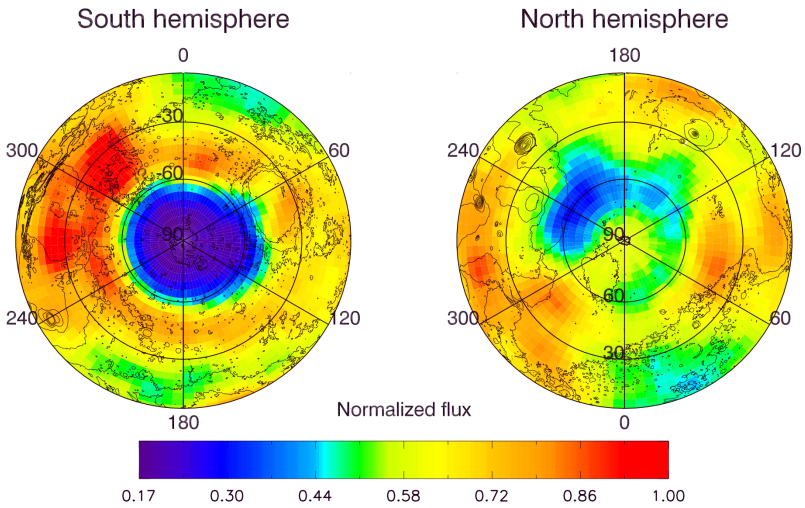

Figure 6. Initial plot of HEND measurements of Mars' superthermal neutron orbit during the first 55 days of mapping at energies ranging from 0.4 eV to 100 keV (adapted from Mitrofanov et al. [52]).

The Fine-Resolution Epithermal Neutron Detector (FREND) onboard TGO is an orbital neutron telescope, capable of detecting hydrogen on the subsurface of Mars up to 1 m depth (Mitrofanov et al. [53]). Mitrofanov et al. [54] analyzed FREND data for the Valles Marineris (VM) region and interpreted the average water-equivalent hydrogen value of Candor Chaos in the central region of VM should be 40.3 wt%. The result points to the presence of water ice permafrost or large amounts of highly hydrated minerals in the subsurface at equatorial latitudes.

The Curiosity rover is equipped with the Dynamic Albedo Detector of Neutrons (DAN), which enables the rover to characterize the soil composition at depths of 0.5–1 m and search for ice and water-bearing minerals beneath the Martian surface (Nikiforov et al. [55], Mitrofanov et al. [56]). This instrument operates by emitting a neutron beam at the surface and then measuring the speed at which the beam reflects. Water and water-bearing minerals are the only hydrogen-containing compounds detected on Mars in significant concentration (Busch and Aharonson [57]). Hydrogen atoms in the subsurface tend to slow down neutrons, and the magnitude of this slowing can indicate the presence of water or ice. Nikiforov et al. [55] proposed a method for estimating the hydrogen content equivalent to water using neutron-sensing data from the DAN instrument on the Curiosity rover and suggested the possible existence of water-containing material in the shallow subsurface of the Vera Rubin Ridge (Nikiforov et al. [55]). In situ radar electromagnetic sounding is also sensitive to the water content of the subsurface, which affects the penetration depth of radar electromagnetic waves. Therefore, this technique can provide important information for other regions of Mars where in situ radar sounding is performed to study the Martian subsurface.

2.4. Soil Analysis

The lander and rover missions were able to analyze the water-ice content of the exploration areas by collecting soil samples or by conducting a direct analysis of soil composition. For example, the Phoenix lander landed in the permafrost zone of the Martian surface and subsequently explored the subsurface ice by collecting soil samples (Smith et al. [58]). Excavations at the landing site revealed the presence of white material beneath the ground (Figure 7), which provides evidence for the presence of liquid brine on Mars (Rennó et al. [9]). The Zhurong rover, equipped with the Mars Surface Composition Explorer, is expected to discover indications of water ice in the Utopian Plainita by directly analyzing the composition of materials in the soil (Li et al. [3]).

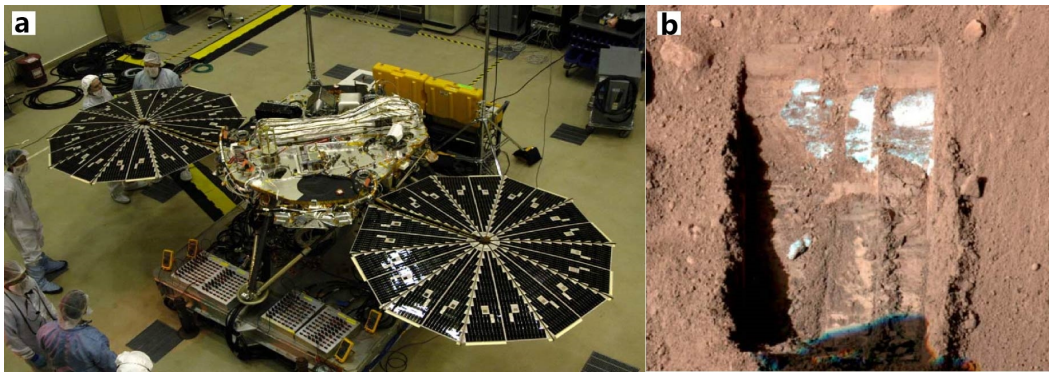

Figure 7. (**a**) Image of the Phoenix lander during the testing phase (adapted from Smith et al. [58]), and (**b**) an image showing the Phoenix robotic arm positioned to excavate the Martian surface. The white area in the image indicates the location of the water ice (adapted from Rennó et al. [9]).

2.5. Other Observation Methods

The widespread presence of clay, rounded gravels, salt patches at lower elevations, and hydrates containing iron compounds, as well as the occurrence of small channels on Mars, all provide evidence of past water flow on the planet (Bibring et al. [59]). The specific minerals found in Martian rocks provide insight into the previous environmental conditions that existed on the planet, including those suitable for life. For instance, the presence of sulfates and water-bearing carbonates in certain Martian meteorites, known as basaltic snow crystals, suggests that they were in an environment containing liquid water before being ejected (Nazari-Sharabian et al. [60]).

The recurring slope lineae (RSL) that form on present-day Mars are characterized by low albedo and are believed to be the result of transient liquid water flow (Stillman et al. [61]). Different parts of Mars produce RSL through various mechanisms, and all slopes containing RSL display evidence of hydrated salts, as shown in Figure 8. Moreover, warm slopes in the Martian seasons can produce liquid water in contemporary Mars (Ojha et al. [62]). Subsequently, through spectral data obtained from OMEGA (Observatoire pour la Mineralogie, l'Eau, la Glace et l'Activite), two forms of water presence on Mars have been identified. They are extensive water ice deposits in the polar regions of Mars and water-containing minerals on the Martian surface, respectively (Bibring et al. [59]). Analysis of near-infrared data from CRISM (Compact Reconnaissance Imaging Spectrometer for Mars) and OMEGA has revealed a widespread distribution of water-bearing minerals on Mars. Specifically, hydrous silicates are primarily distributed in the south highlands, while water-bearing minerals in the northern lowlands exhibit greater compositional diversity and are found in various geological epochs (Bibring et al. [59]). This indicates that the forms of water present on Mars are highly diverse and span multiple geological eras.

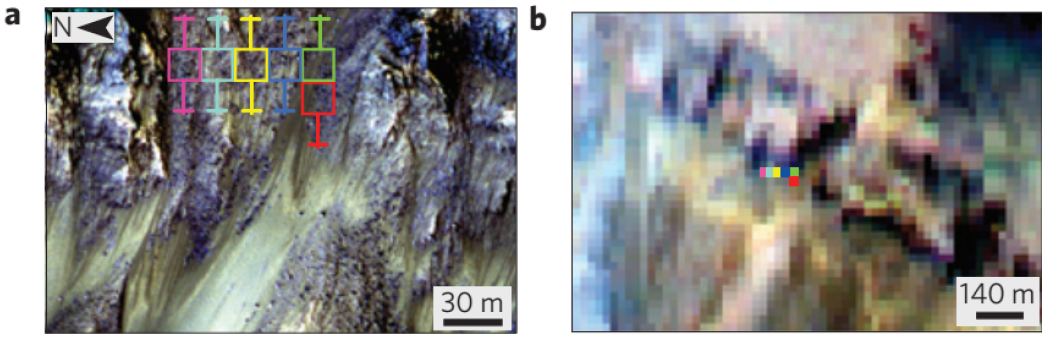

Figure 8. Recurring slope lineae in Palikir Crater (adapted from Ojha et al. [62]). (**a**) Infrared images of RSL on the slope of Palikir Crater. Colored boxes indicate the uncertainty of CRISM pixel locations; (**b**) synchronized CRISM observations.

In mineralogical surveys, it has been found that water-bearing minerals on Mars are mainly composed of Fe/Mg smectites, chlorite, and hydrated silica (Carter et al. [63]). Most of these water-bearing minerals formed before the middle of the Noachian, with a smaller portion continuing to form into the Hesperian and early Amazonian. Subsequent analysis, through crater age dating, has revealed that water-bearing minerals predominantly formed during the Noachian and the early period of Hesperian. The formation of these minerals decreased during the late Hesperian and Amazonian. Analysis of water-bearing minerals within impact melt materials inside craters has confirmed the presence of groundwater or previously existing hydrated minerals, subsurface ice, and impactor ice throughout Mars' history (Sun and Milliken [64], Wernicke and Jakosky [65]).

Based on estimations of the global water content on Mars, the water stored in and required for the formation of water-bearing minerals is estimated to range from 130–260 m of Global Equivalent Layer (GEL), with a theoretical range of 70–860 m GEL (Wernicke and Jakosky [65]). The estimated global water equivalent on Mars falls between 173–317 GEL, with a potential range of 110–1114 m GEL (Wernicke and Jakosky [65]). This underscores the significance of water-bearing minerals as a crucial reservoir of water on Mars, providing valuable insights for future endeavors in detecting water ice reserves and extracting water resources on the planet Mars.

3. Evidence for the Past Presence of Water Ice in the Shallow Surface

The past existence of water in the shallow surface layers of Mars is strongly supported by the existence of various geological formations, including canyons, outflow channels, oceans, washes, riverbeds, and lake basins. (McEwen et al. [11]). The analysis of these features sheds light on the planet's geological evolution, providing insights into past crustal activity and the climatic environment of Mars. Currently, remote sensing photography, terrain exploration, and mineral analysis are the primary methods for identifying and analyzing geological features on Mars. The Martian surface is primarily composed of basalt, a type of fine-grained magmatic rock comprising plagioclase, pyroxene, and the basal silicate mineral olivine, which can combine with water to form crystalline structures during chemical weathering (Ehlmann and Edwards [66], Yen et al. [67], Chevrier and Mathé [68]). The formation of secondary minerals requires water, and although they generally do not contain water themselves, they can serve as evidence to determine the past presence of water in the shallow surface layers (Craddock and Howard [69]).

3.1. Canyon Network Features

Branching channel systems, also called canyon networks, on Mars have been considered some of the strongest evidence for past water flow on the surface of Mars (Carr and Chuang [70]). These valleys bear similarities to river valleys found on Earth. To understand the origins of the river channels on Mars, scientists compared the density of craters on Earth and Mars with the density of the Martian river network. They concluded that valley formation on Mars likely involved slow erosion by flowing water over a short duration. The rock structure of Mars differs significantly from that of Earth (Carr and Chuang [70]). Viking observations suggest that during the Noachian period, upland grading was a long-term, slow process with possible brief periods of strong erosional fluvial activity from the late Noachian to early Hesperian, which resulted in an immature valley network. Martian global river valley drainage age densities were mapped using Mars Odyssey spectral data with Viking Mars images (Figure 9), and a high correlation was found between high drainage densities and river sediments (Hynek et al. [71]). The widespread distribution of hypothetical ancient lakes, fan delta sediments, and chlorides detected by THEMIS data indicates that most of Martian valleys and associated sediments were attributed to prolonged surface precipitation runoff.

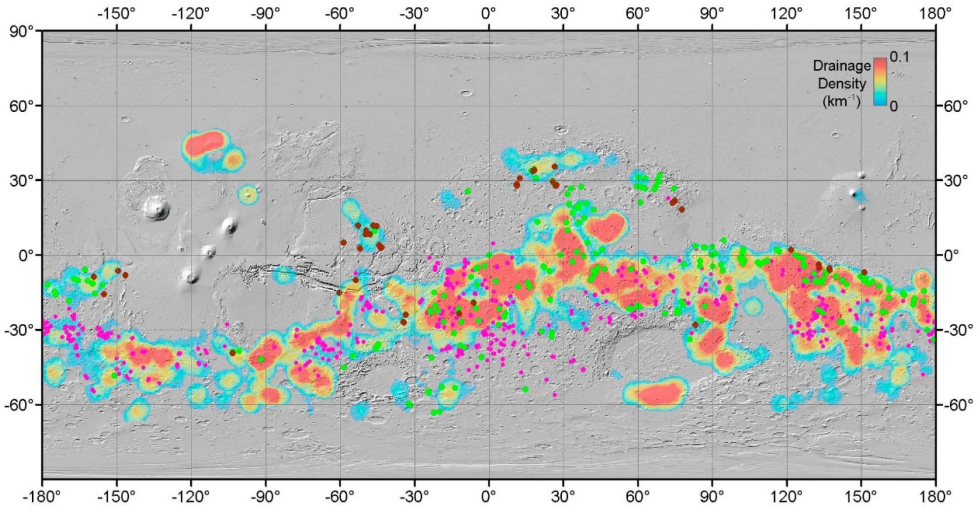

Figure 9. Map of the density distribution of full Martian river valleys, along with the distribution of river valleys on Mars that are believed to have ancient lake deposits (indicated by green circles, (adapted from Fassett and Head III [72]), fan deltas (shown as dark red circles, (adapted from Di Achille and Hynek [73,74]), and chlorine deposition (represented by pink circles).

Additionally, a climate model for ancient Mars, a 3D simulation of climate for the late Noachian and early Hesperian periods, and a river transport model were developed (Kamada et al. [75]). These models revealed that a CO_2 atmosphere, with a small amount of hydrogen at surface pressures exceeding two bar, could generate an environment conducive to the presence of stable liquid water on the surface. This would explain the observed distribution of certain valley networks, which can be attributed to river runoff. It suggests that the Martian valley networks may also be due to seasonal or transient snowmelt (Kamada et al. [75]).

3.2. Paleolake Features

Both on Earth and Mars, lakes are areas of high atmospheric activity and energy flow at the intersection of the hydrosphere, lithosphere, and cryosphere, making ancient Martian lakes a key target for Mars exploration. In recent years, the Spirit, Curiosity, and Perseverance rovers have landed in Gusev Crater, Gale Crater, and Jezero Crater, respectively, all of which have been identified as, or are believed to be, sites of paleolake (Farley et al. [46], Golombek et al. [76], Grotzinger et al. [77]). Over 400 paleolake basins have been identified on Mars using remote sensing techniques and can be divided into three categories: valley network-fed closed-basin lakes (Figure 10a), isolated inlet valley closed-basin lakes (Figure 10b), and valley network-fed open-basin lakes (Figure 10c). These findings suggest that the early Martian paleolake basins required a significant inflow of water to become filled and submerged (Goudge et al. [78]). To date, there is sufficient evidence confirming the presence of approximately 500 ancient lakes on Mars, as observed through visible imaging, infrared imaging, multispectral hyperspectral analysis, and stereo imaging (Figure 11) (Michalski et al. [12]).

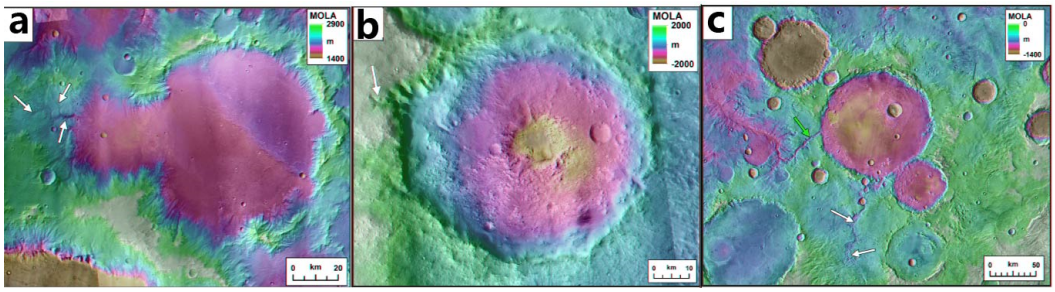

Figure 10. Examples of paleolakes on Mars (adapted from Goudge et al. [78]). White arrows indicate inlet valleys and green arrows indicate outlet valleys. (**a**) Valley network-fed closed-basin lake at −11.3°N, 131.4°E. (**b**) Isolated inlet valley closed-basin lake at 21.4°N, 58.1°E. (**c**) Valley network-fed open-basin lake at −10.6°N, 2.8°E.

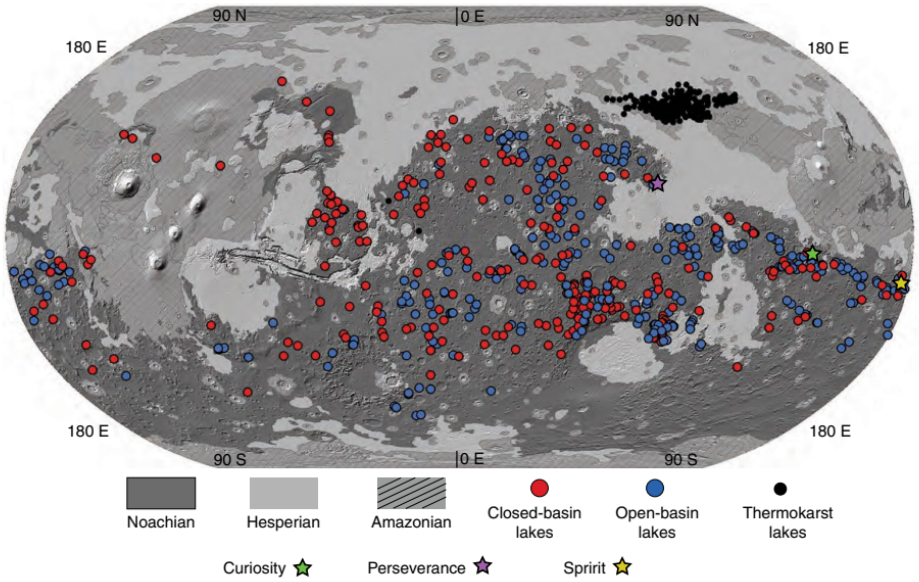

Figure 11. Global distribution of lake basins on Mars (adapted from Michalski et al. [12]).

The detection of paleolakes in the diverse landscapes of Mars has been of great significance in the present time. To examine the hypothesis of the presence of paleolakes, sediment analysis was conducted on the crater interiors of five craters (Figure 12) larger than 10 km in diameter situated in the westernmost lobes of the Medusae Fossae Formation (Aeolis and Zephyria Planum), approximately 800 km east of Gale Crater (Burr et al. [79]). A sedimentary unit with wind-formed paleoenvironment and fluvial paleoenvironment as the main supporting features were eventually identified, with another possible lacustrine sedimentary paleoenvironment (Peel and Burr [80]), providing a basis for later verification of the paleolakes. Moreover, the Jezero crater is also believed to be a paleolake at the Perseverance landing site (Farley et al. [46]). The RIMFAX radar carried on its Mars rover is expected to detect direct evidence of water ice in the area of the paleolake.

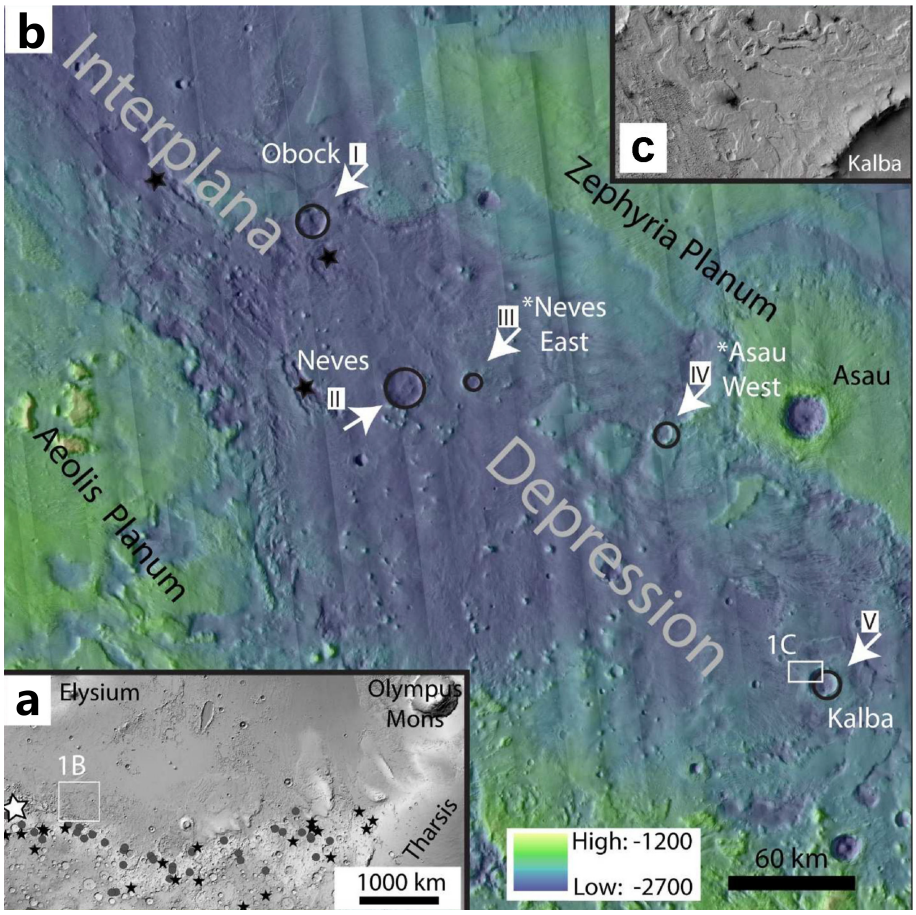

Figure 12. Part of the Medusae Fossae Formation region spanning the western Tharsis and eastern Gale crater, with black circles indicating impact crater lakes, adopted from Peel and Burr [80]. (**a**) MFF region of Mars, spanning the dichotomy boundary west of Tharsis and east of Gale crater (white star) and showing the locations of catalogued crater lakes that overflowed, forming an outlet channel (circles) and those that did not (black stars) on MOLA grayscale. Figure 1B in original paper represent Figure 12b in this paper. (**b**) Aeolis Dorsa region of Mars shown in CTX images with MOLA colorshade overlay. The craters mapped in this project are outlined with black circles and labeled by roman numerals and formal and ∗informal names. Figure 1C in original paper represent Figure 12c in this paper. (**c**) portion morphology of Kalba crater.

3.3. Marine Remains

Besides paleolakes, the presence of primitive oceans covering over 30% of the Martian surface can be inferred by exploring the hydraulic and thermal characteristics in the source areas of the Late Hesperian outflow channels and comparing them with the topographic and geomorphological evidence. It is suggested that these oceans once occupied the present northern plains of Mars (Clifford and Parker [10]). Measurements of the dielectric constant of the Vastitas Borealis Formation (VBF) within the shoreline of the paleo-ocean by MARSIS radar, which reveal that the VBF has a low dielectric constant (Figure 13), indicating that it is sediment or sediment mixed with significant amounts of ice deposited from water, supporting the claim of the existence of the northern paleo-ocean (Mouginot et al. [81]).

The Zhurong rover's Surface Composition Explorer has examined the VBF soil composition of the Utopia Plain. Through the utilization of laser-induced breakdown spectrometry (LIBS) and shortwave infrared spectroscopy (SWIR) to compare the spectra of opal, allophane, imogolite, and pyroxene from the RELAB database with the spectra of six selected VBF target layers (see Figure 14), it has been determined that the soils at the Zhurong rover landing site are a mixture of igneous minerals containing allophane and imogolite/opal, which have undergone minimal chemical alteration. These sediments are believed to have

formed due to extensive erosion of volcanic clastic soils in a cold environment with short-lived water (Liu et al. [82]). Xiao et al. [83] reported the first in situ observations of VBF and interpreted the layered features as sedimentary structures typical of marine environments detected by the Zhurong rover.

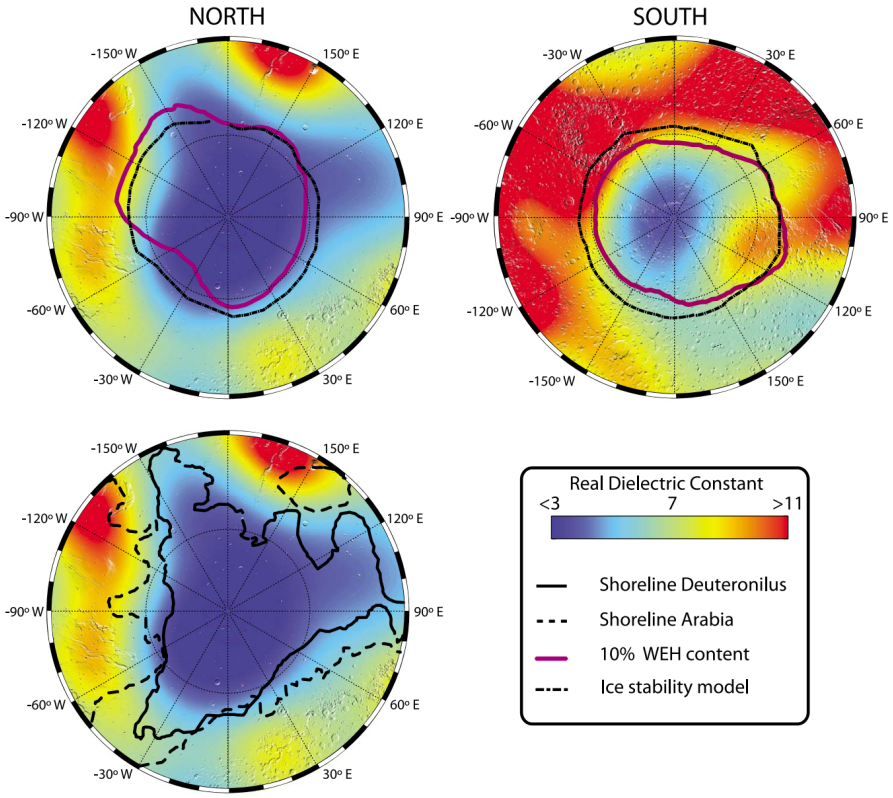

Figure 13. Distribution values of dielectric constants on the surface of Mars from MARSIS radar inversions (adapted from Mouginot et al. [81]).

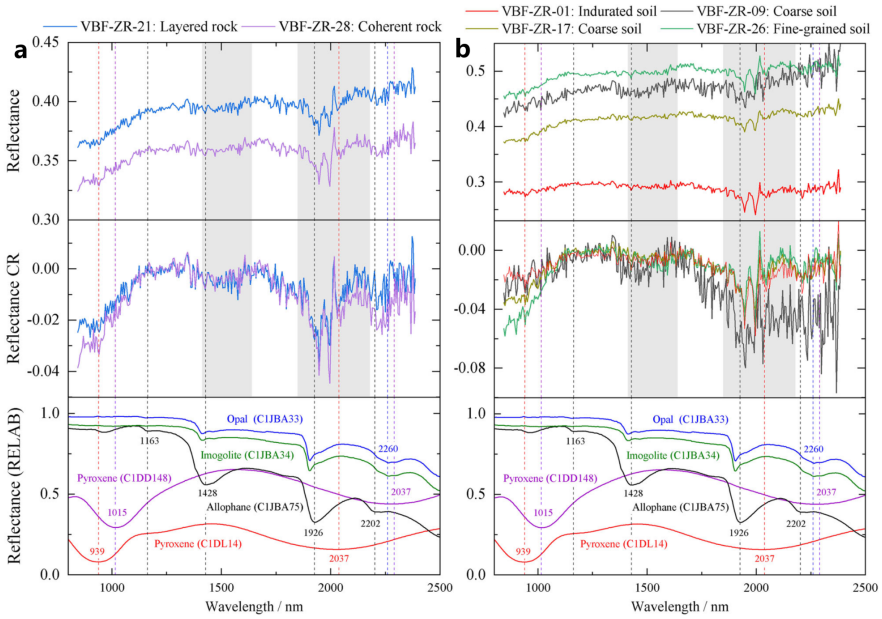

Figure 14. SWIR absolute spectra and mineral identification maps (adapted from Liu et al. [82]). (**a**) selected VBF rocks; (**b**) selected VBF soils (reflectance CR is the spectrum after removal of the continuum, the dashed lines indicate the absorption centers of these phases and the grey areas indicate the absorption features of the Martian atmosphere).

3.4. Rampart Craters and Polygonal Terrain

There is a unique type of impact crater known as the rampart crater on Mars. These craters exhibit multiple layers of continuous ejecta deposits (Carr et al. [84], Osinski [85], Mantegazza et al. [86]). The surface of the ejecta deposits features closely spaced radial stripes, discontinuous concentric ridges, and steep troughs. What makes them particularly distinctive is that each layer of ejecta is bordered by a low ridge or cliff extending from the crater's rim to a distance equal to twice the crater's diameter. This layered arrangement resembles successive barriers encircling the crater, hence the name rampart crater (Carr et al. [84], McCauley [87], Wulf et al. [88]). The formation of these rampart craters is explained by the presence of permafrost or subsurface water in the impacted region, which imparts fluidity to the ejected material (Carr et al. [84,89]). By simulating impacts on mixtures of ice and rock, it has been observed that the resulting craters display elevated ejection angles, fluidized ejecta blankets, and increased crater uplifts. This serves as further evidence supporting the role of water ice in the creation of rampart craters (Stewart et al. [90]). In the northern plains region of Mars, there are extensive polygonal terrains, which are cut by complex grooves and fissures ([89,91]), these polygonal terrains are primarily found in low-lying areas where evident deposits exist on Mars. Several hypotheses have been proposed for the formation mechanism of these polygonal terrains, e.g., the disappearance of water body loads leading to ground uplift and deformation, infiltration of surface water into frozen soil fissures resulting in the formation of ice wedges combined with the drying process, and the shrinkage of dry sediments and the cooling of volcanic rocks (Helfenstein and Mouginis-Mark [92], Hiesinger and Head III [93], McGill and Hills [94], Pechmann [95], Seibert and Kargel [96], Wenrich and Christensen [97]). On a smaller scale, the likelihood of mud-dry crack formations, contraction from cooling lava, or thermal contraction cracks is higher, and this cracking mechanism is closely related to fine-grained materials rich in water ice, indicating the presence of seasonal liquid water traces on the Martian surface (Seibert and Kargel [96], Mellon [98]). It is worth noting that impact craters on the polygonal terrains exhibit the morphology of rampart ejecta (Hiesinger and Head III [93]).

According to the radar data of Zhurong, it was found that there existed a wide distribution of buried polygonal terrain under Utopia Planitia. These polygons are interpreted as being produced by freeze-thaw cycles, where thermal contraction cracks first, and then water or soil material fills the cracks (Zhang et al. [17]). Wang et al. [99] investigated the transverse aeolian ridges (TARs) in the Zhurong landing region and identified polygonal features with hydrated minerals. They proposed the possible formation mechanisms of the polygons were contractional cracks formed during groundwater evaporation or fracture of indurated sand crust and the latter is the most possible mechanism. Either way, it may be related to recent water activity and atmosphere–surface water exchange on Mars.

Therefore, based on speculation regarding the formation mechanism of the rampart craters and the polygonal terrains, they can be considered significant evidence of the past presence of liquid water, interstitial water, or water ice on the Martian surface. These landforms, widely found in Utopia Planitia and Argyre Planitia, are also preferred landing areas for various countries' Mars exploration missions to investigate water ice (Seibert and Kargel [96], Liu et al. [100]). It is expected that the ground-penetrating radar carried by the Zhurong rover will detect such impact craters along its traverse route and conduct more in situ investigations of the distribution and properties of water ice beneath the Martian surface.

3.5. Other Surface Geological Features

Several distinctive characteristics can be also indicative of past water presence on Mars. The widespread occurrence of rootless volcanic cones and cratered terrain in the Tartarus colles region suggests the existence of a significant fossil hydrothermal system. The evolution process of this lava–ice interaction is as follows: At the beginning, the Tartarus colles lava flow is situated above a basement containing ice. The concentrated flow of lava towards the central path resulted in a thickness of approximately 60 m in the central location, while the edges of the

lateral flow remained around 30 m thick. (Hamilton et al. [101]). The heat of the lava melted the ice in the basement, causing the lava to sink and form a deformable base. Heat transfer from the lava to the basement allowed water to gradually escape and form a space beneath the lava. Eventually, the lava collapsed into the basement, along with fragments of the rootless cone, creating the observed features (Hamilton et al. [101]). This hydrothermal system was formed through interactions between lava and surface ice during the late to mid-Amazonian period, indicating the presence of water ice on Mars during this period (Hamilton et al. [101]). The use of ground-penetrating radar, especially the Mars in situ detection equipment, enables the detection of water ice beneath the surface of this geological feature.

In 2022, hydrated sulfate/silica material was identified in the Amazonian strata at the landing site through short-wave infrared spectroscopic data collected by the Zhurong rover in southern Utopia Planitia. These materials were interpreted as crusts that formed in situ and suggested that strata containing large amounts of liquid water formed as a result of groundwater uplift or melting. Evidence at the Zhurong rover landing site also suggests that the Amazonian hydrosphere on Mars is more active than previously thought (Liu et al. [102]).

The radar data from the RoPeR has unveiled subsurface layering in the Utopia basin of Mars, pointing to sedimentation resulting from intermittent hydraulic flooding. This is interpreted as representing the infilling of Utopia Planitia during the Late Hesperian to Amazonian periods (Li et al. [26]).

A recent work using LIBS onboard the Zhurong rover is analyzing the surface targets of the landing zone. The lithified duricrusts were detected to have a high water content. The cemented duricrusts may be formed through water vapor-frost cycling at the atmosphere–soil interface, and soils and sands contain hydrated magnesium salts and adsorbed water. Those evidences indicate potential Amazonian brine (Zhao et al. [103]).

Zhurong rover also observed some surface features inferred to have formed 1.4 to 0.4 million years ago in the southern Utopia Planitia, which includes cracks, aggregates, bright polygonal ridges, and crusts. These geological features are most likely caused by saline water from thawed frost/snow (Qin et al. [104]).

In the transitional area between Elysium and Utopia Planitia, significant deposits of material with a relatively high albedo have been observed. This material is located in extensive deposits around terraces, in cratons, and valley systems. It is believed that these deposits consist of modified ice-rich material, lineated valley fills, lobate debris aprons and degraded deposits of concentric crater fill. The presence of degraded ice-rich sediments at all elevations and latitudes in the study area suggests that ice-mantle material was originally deposited over a wide area and remained stable for a long period. Long-term sediment interaction processes are hypothesized to have ultimately played a part in forming the transition zone between Elysium and Utopia Planitia (Pedersen et al. [33], Pedersen and Head [35]).

The glacial and periglacial landforms on Mars are also a form of water storage. Rock glaciers (lobate-shaped landforms of unconsolidated sediment and rock debris) may have evolved from glaciers. Williams et al. [105] compiled morphometric data from the lobate feature on Mount Sharp (the northern slopes of Aeolis Mons), using orbitally derived imagery of HiRISE and CTX. These lobate features are evaluated as terrestrial rock glacier analogs. The periglacial features on Mount Sharp suggest the existence of water for the production of ice in the past equatorial region (Williams et al. [105]).

4. Evidence for the Current Presence of Water Ice in the Shallow Surface

The current presence of water ice has significant implications for studying the Martian climate's evolution and habitability for human exploration. Mellon predicted the distribution of water ice on Mars based on thermal inertia, albedo, and insolation calculations, which led to the conclusion that subsurface ice is stable in the high inclination range but not stable in the low inclination range (between $\pm 60°$) (Mellon and Jakosky [106]). As Mars exploration missions have progressed, NASA's Mars Odyssey, Curiosity, Perseverance, and China's Tianwen-1 have deployed advanced equipment such as spectrometers and radar. Recent Mars exploration missions will provide more evidence to find water ice in the shallow subsurface of Mars.

4.1. In Situ Spectrometer Detection

Since hydrogen atoms block high-energy cosmic rays, the absence of high-energy neutrons produced by cosmic rays on Mars indicates a widespread subsurface distribution of hydrogen elements, presumably present in water ice (Mitrofanov et al. [52]). Subsequently, the Thermal Emission Imaging System (THEMIS) onboard Mars Odyssey made a noteworthy finding of water ice, which was distributed near the periphery of the southern perennial polar cap of Mars. Daily and seasonal temperature trends on Mars based on observations from THEMIS suggest the presence of water ice on the Martian surface. Combined with Viking observations and a small number of other relevant observations from THEMIS, water ice on the Martian surface may be widely distributed around and beneath a perennial carbon dioxide ice cap (Titus et al. [107]). This result coincides with HEND's detection of large amounts of hydrogen in the southern polar subsurface (Mitrofanov et al. [52]).

Possible signs of liquid water on the Martian surface include recurring slope lineae observed on sloping terrain. These recurring slope lines (RSLs) (Figure 15) appear and gradually lengthen on low albedo surfaces during the warm season, which is observed as a narrow, dark mark on steep slopes (Stillman et al. [61]). RSL fades out during the cold season and occurs repeatedly in multiple Martian years (the statistical period ranges from Mars year 28 to 32). Data analysis from MRO has revealed the extensive occurrence of RSLs in the equatorial regions of Mars, particularly in the deep valleys of VM. RSLs are most active during seasons when the slopes are often facing the Sun. The abundance of RSLs in VM indicates a higher concentration of liquid water close to the surface in the equatorial region, surpassing the predictions of equilibrium models. This assumption is based on the association of RSL abundance in VM with the presence of flowing water (McEwen et al. [13]). This finding suggests that the high value of mean water equivalent hydrogen detected by FREND (Mitrofanov et al. [54]) is probably caused by the abundance of RSLs. Containing huge volumes of fossil ice from ancient glaciers, VM also has fossil glacial land systems, probably contributed by accumulated ice of chasma floors and valley walls at low elevations. And wet-based glaciers can flow and slide over the bed of the glacial system (Gourronc et al. [108]).

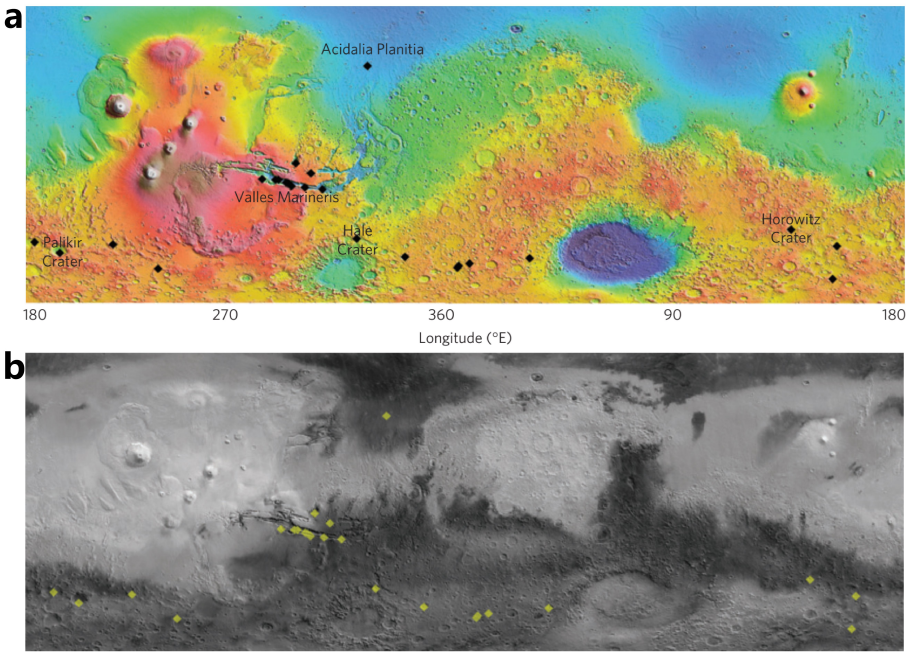

Figure 15. Locations of confirmed recurring slope lineae (RSLs) (adapted from McEwen et al. [13]). (**a**) Locations of confirmed RSLs as black diamonds; (**b**) the same set of RSLs on the Thermal Emission Spectrometer global radiative heat albedo map as yellow diamonds.

In 2020, discoveries of water ice on steep walls within two craters in the northern mid-latitudes of Mars were reported based on high-resolution images and spectral data from the Mars Reconnaissance Orbiter (Figure 16) (Vijayan et al. [109]). The exposed water ice deposits were shallow, with absorption bands at 1.5 μm and 2 μm, and the exposed ice remained stable after a 1-week interval in one location. It complements earlier research indicating the wide distribution of shallow water ice on Mars and aligns with the detection of subsurface water ice by the Neutron Star Spectrometer. The final interpretation is that the presence of shallow surface water ice in the origin deposits of polar-facing and equatorial-facing Martian rock walls in mid-latitude craters in the Northern Hemisphere implies the potential abundance of water ice resources in the shallow surface layers of Mars (Vijayan et al. [109]). Butcher [110] further summarized water ice at mid-latitudes on Mars: water ice is present as regolith and deposits of excess ice with bigger volume; most of the known excess ice deposits were probably formed under climatic conditions within the last few million to 1 billion years.

Currently, in situ spectrometers on Mars are more oriented towards detecting the abundance of water vapor in the Martian atmosphere and analyzing the distribution of water in the Martian atmosphere and climate change. For example, the "Nadir and Occultation for Mars Discovery" spectrometer suite (NOMAD) is designed to investigate the composition of Mar's atmosphere (Vandaele et al. [111]); CRISM is designed to measure spatial and seasonal variations in the atmosphere (Murchie et al. [112]). Spectrographic analysis remains the most convincing evidence for water ice and water-bearing minerals exposed outside or near the surface of Mars.

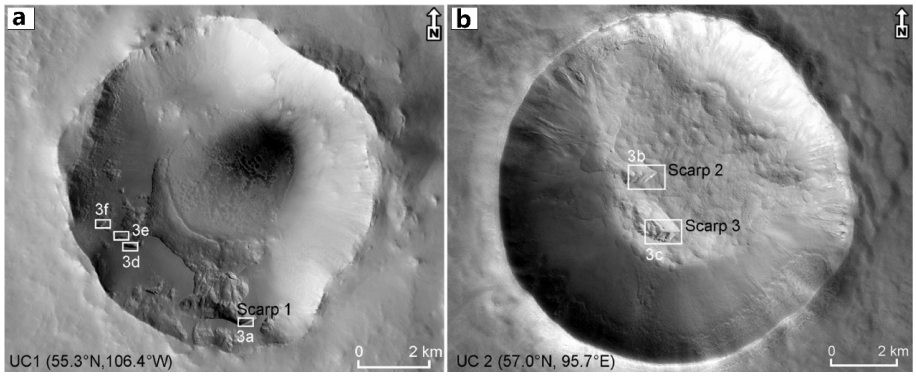

Figure 16. Two unnamed craters in the northern lowlands of Mars, referred to as UC1 and UC2 (adapted from Vijayan et al. [109]). (**a**) Crater UC1 with steep slopes on the polar face wall. Picture 3a/b/c/d/e/f are relative to original paper (Vijayan et al. [109]). (**b**) UC2 crater with steep slopes on the floor.

4.2. Radar Observation

The primary types of radar currently available for observing Mars are Mars-orbiting penetrating radar and the in-situ ground penetrating radar (Zhou et al. [15], Seu et al. [21], Hamran et al. [25]). Those two kinds of radars can detect the thickness and stratification of the Martian soil beneath the surface, as well as the distribution of water ice. MARSIS, SHARAD, and MOSIR are orbiter penetrating radars currently in operation on Mars, and the rovers Perseverance and Zhurong carry the in situ ground-penetrating radars.

MARSIS recently detected bright reflections at the base of SPLDs. Orosei et al. [44] suggested these indicate liquid water due to lowered freezing points from high brine concentrations. Lauro et al. [113] then identified multiple reflections, proposing the presence of multiple liquid water bodies. However, some researchers dispute this, citing temperature and heat flux limitations, suggesting the different dielectric properties of minerals or clay as potential causes (Ojha et al. [114], Bierson et al. [115], Smith et al. [116]). Layered interference within the SPLDs and high-density igneous material with metallic inclusions are also thought to cause (Lalich et al. [117], Grima et al. [118]). Laboratory

experiments have been conducted to measure the dielectric properties of relevant materials under similar conditions, and materials like clay cannot produce such bright reflections (Mattei et al. [119], Cosciotti et al. [120]).

To determine resources available for human exploration of Mars, NASA is promoting the Mapping Project (SWIM), which aims to map the water ice resources on Mars (Bain et al. [121]). The ice resources of the Deuteronilus Mensae region were mapped through SHARAD's radar analysis of glacial and mantle sediments. The results show an average dielectric constant of 3.4 $\pm$ 0.5 for ice and 4.0 $\pm$ 1.0 for mantle sediments in the region. A newly developed radar surface analysis technique was used to compare the mantle and glacier units. It was found that the radar surface analysis on the mantle unit (see Figure 17) resulted in higher return power than on the glacier (Morgan et al. [122]).

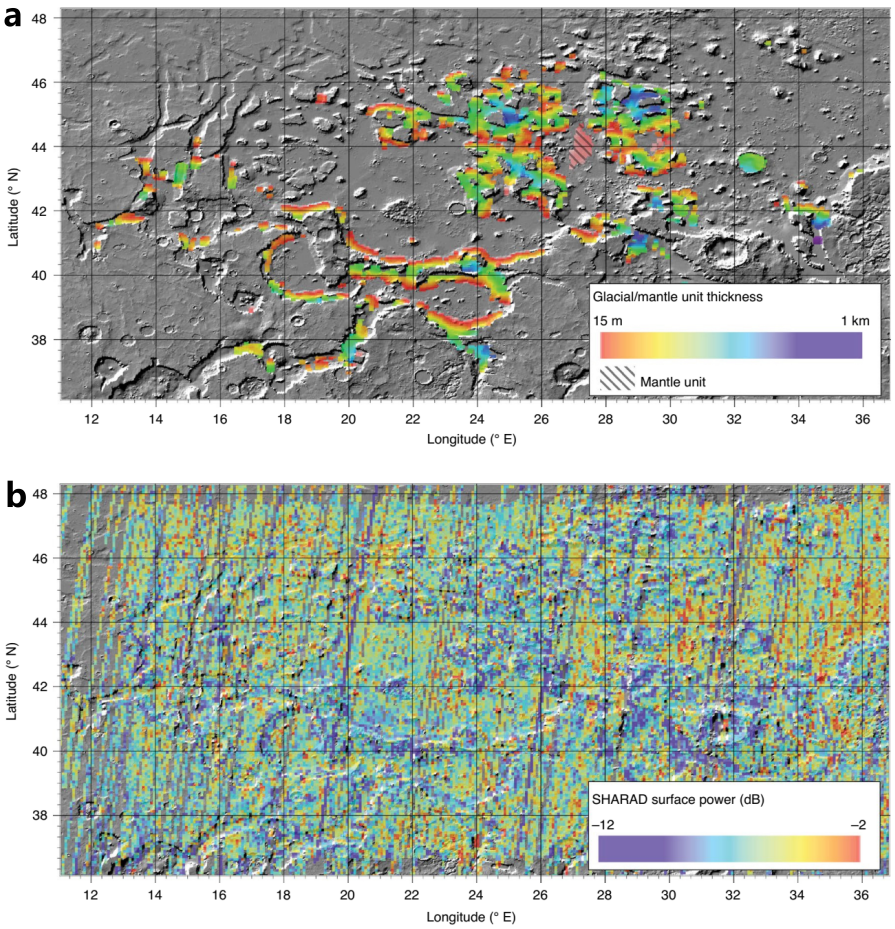

Figure 17. Radar analysis of glacial and mantle deposits within the Deuteronilus Mensae region (adapted from Morgan et al. [122]). (**a**) Depth of glacial sediment and mantle unit to the basement. (**b**) Regional correspondence radar surface analysis. Notably, the low power returns, which are consistent with the presence of ice above 5 m, are associated with the glacier surface.

Regarding the exploration of water ice on Mars, investigations in the polar regions of Mars have revealed extensive ice caps, similar to those at Earth's poles, with thicknesses reaching up to several kilometers (Farrell et al. [123], Grima et al. [124], Levrard et al. [125], Zhou et al. [126], Garvin et al. [127], Putzig et al. [128]). In the southern polar region, due to the thick ice layer, deep reflection signals could not be detected by SHARAD. However, in the region spanning from 310° E to 0° E, MARSIS detected a reflection layer with a thickness of approximately 3.7 km. This layer is interpreted as the boundary between ice-rich south-polar layered deposit materials and the bedrock (Plaut et al. [129]). In the northern polar region, both MARSIS and SHARAD radars detected reflection signals indicating the

boundary between the ice layer and the substrate (Picardi et al. [19], Phillips et al. [130], Putzig et al. [131]). In the mid-latitude regions of Mars, as temperatures rise, surface water ice sublimates, revealing various forms of water ice in different areas, such as glacier deposits in the eastern part of the Hellas basin, abundant water ice in the Deuteronilus Mensae region, and extensive subsurface ice water in the Utopia Planitia (Bramson et al. [43], Stuurman et al. [132], Plaut et al. [133]). Dundas et al. [134] through comparative analysis of high-resolution images combined with radar data analysis, discovered substantial water ice at eight different cliff locations in mid-latitude regions of Mars, extending from depths of 1 to 2 m to over 100 m thick. However, the question of whether water ice exists in lower latitude or equatorial regions of Mars has long intrigued scientists. The Medusae Fossae Formation is a unique, young deposit spanning thousands of kilometers along the equator of Mars, the structural origin of which remains unclear. Both MARSIS and SHARAD radars have probed this region, with Watters et al. [135] calculating an electromagnetic attenuation coefficient of $\sim$0.0048 ± 0.0024 dB/m and a dielectric constant of $\sim$2.9 ± 0.4 using MARSIS data orbit 02896, suggesting that the dielectric properties of this region are similar to pure water ice, although the possibility of dry, low-density materials such as volcanic ash cannot be ruled out. Carter et al. [136] calculated electromagnetic attenuation and dielectric property parameters using SHARAD radar data in this region, essentially obtaining research results similar to those of Watters et al. [135]. Recent studies have reported a significant presence of underground water ice in the Medusae Fossae Formation on Mars Campbell et al. [137], Watters et al. [138], although further research is still needed.

5. Shallow Subsurface of the Perseverance Landing Site

Perseverance is the centerpiece of NASA's 2020 Mars mission (Figure 18), carrying a set of scientific instruments to interpret the geology of the landing site, detect potential biological features, collect and record Martian rock and soil samples, and map the near-surface Martian environment (Farley et al. [46]).

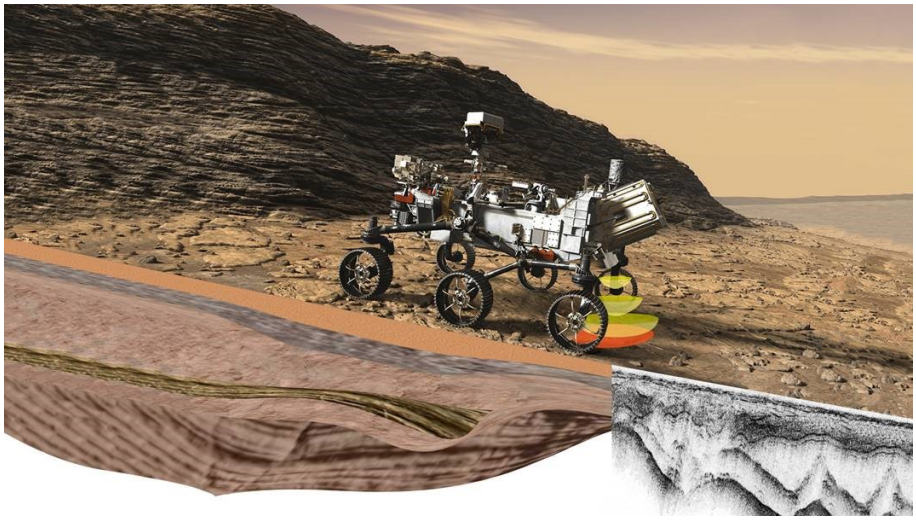

Figure 18. Martian-based ground-penetrating radar, RIMFAX onboard Perseverance rover. Credit from NASA/JPL-Caltech/FFI.

Of these instruments, RIMFAX is a ground-penetrating radar that operates within the frequency range of 150 MHz to 1200 MHz, utilizing frequency-modulated continuous wave technology. It possesses the capability to observe at different depths over a dynamic range of approximately 100 dB (Hamran et al. [14]). Shallow imaging with full bandwidth (effective center frequency of 675 MHz) is used to image the subsurface to a depth of a few meters, while deeper imaging with lower bandwidth (center frequency of 375 MHz) is used for deeper ranges. RIMFAX is designed to study the stratigraphic structure and dielectric properties of the subsurface layers in the landing zone, and the depositional sequences

observed by the radar will provide information for the study of the subsurface stratigraphy of the landing area (Hamran et al. [14,25], Farley et al. [46]).

On 18 February 2021, the Perseverance rover successfully landed in the Jezero crater, which is located in the Nili Fossae region of Mars (Hamran et al. [25]). The Jezero crater, formed in the mid to late Noachian period, has a diameter of about 45 km (Goudge et al. [139]). Orbiter observation identified two river valley networks forming an alluvial fan to the west and one to the north in the Nili Fossae region (Figure 19). They suggested that the climatic conditions in the Noachian Nili Fossae region could have supported the flow and accumulation of liquid water on the surface (Fassett and Head III [140]). This is one of the reasons why Perseverance chose the Jezero crater as its landing site. After the Perseverance rover landed, images of the western sedimentary fan (Figure 20) were obtained using remote microimaging with the Mastcam-Z camera and SuperCam instrument. These images revealed the presence of hills (Kodiak) on the sedimentary fan that was invisible from orbit. The hills were interpreted as erosional remains of an originally more extensive fan deposit, with overall stratigraphic features suggesting an incoming western deltaic system and a long-term retreat of the lake level (Mangold et al. [141]). The presence of inclined strata in the hills can thus be interpreted as evidence that the sedimentary fans here are lacustrine deltas (Mangold et al. [141]).

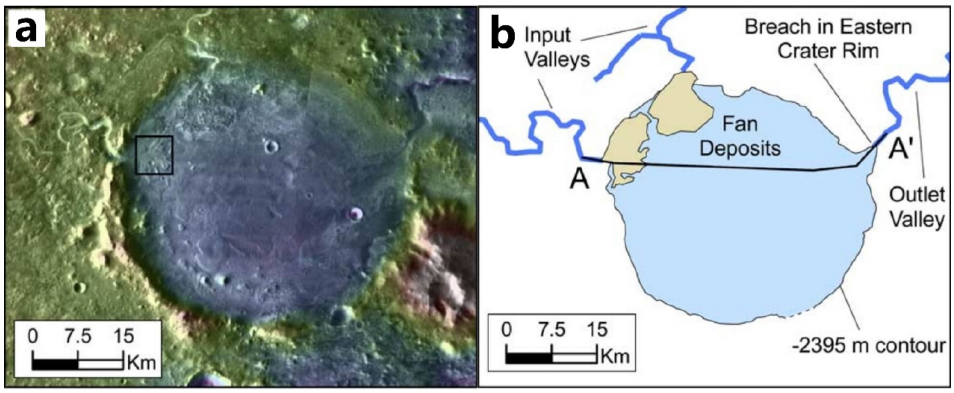

Figure 19. (**a**) Image of the Jezero crater and its alluvial fan, and (**b**) the two inlet valley networks and one outlet valley network of the crater, as identified in a previous study (adapted from Fassett and Head III [140]).

There is an interesting observation regarding the uppermost fan stratigraphy at the Jezero crater, which is composed of boulder conglomerates indicating intermittent high-energy floods. This suggests a shift from continuous hydrological activity in a persistent lacustrine environment to a high-energy, short-duration fluvial flow. Furthermore, Mastcam-Z images and multispectral data of the rocks at the floor of the Jezero crater revealed their morphology, lithology, and mineralogy to be consistent with lightly aqueous altered igneous rocks that have undergone varying degrees of local impact damage. Wind metamorphism has then formed superficial fine-grained soil material containing evidence of pyroxene, olivine, and crystalline hematite (Bell III et al. [142]).

After the Perseverance rover's initial exploration of the Martian subsurface, electromagnetic properties, and bedrock stratigraphy were obtained at a depth of 15 m below the surface of Jezero Crater (Hamran et al. [25]). The radargram was segmented by defining 286 marker points during the nearly 3-kilometer journey of the rover. The travel path (Figure 21a), the radargram (Figure 21b), and the cross-sectional interpretation (Figure 21c) correspond to the journey from sol 201 to 202 (Hamran et al. [25]). Strongly reflective layers that dip from the surface to a depth of about 15 m are associated with erosion-resistant rock outcrops parallel to the Artuby Ridge, and these reflective layers, along with the dip layer represented by the surface ridge, are the Séitah Formation's outermost layer. A zone of lower reflectivity exists between the strongly reflective layers, which is interpreted as a zone of sediment from the dust weathering layer (Hamran et al. [25]).

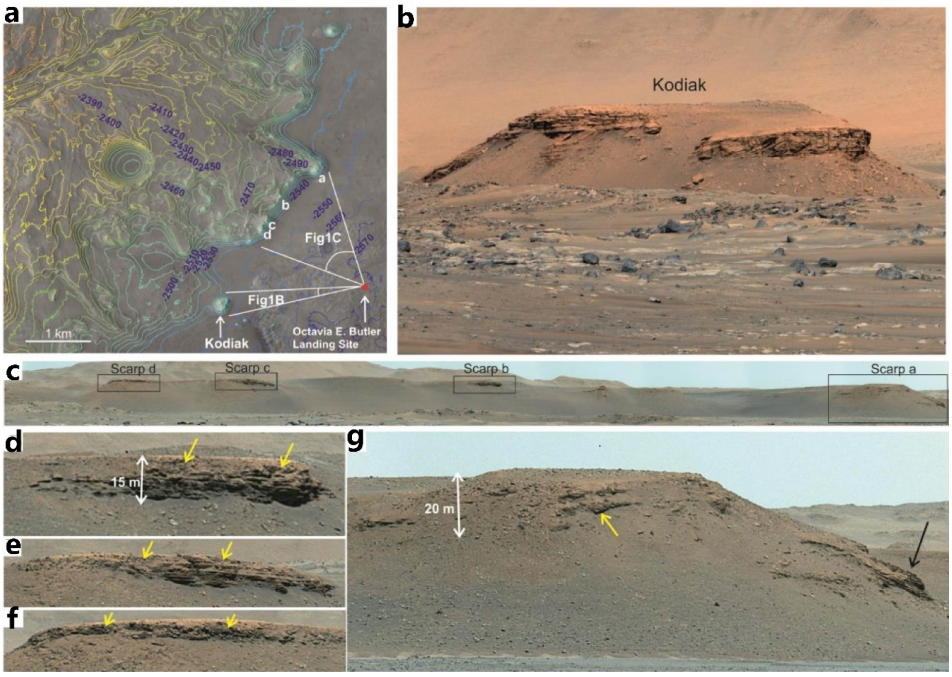

Figure 20. The topography of Jezero Crater as observed by the Perseverance rover (adapted from Mangold et al. [141]). (**a**) The High-Resolution Imaging Science Experiment (HiRISE) data, which display the western fan and the landing site located in the interior of Jezero Crater, are referred to as Octavia E. Butler (indicated by the red dot). Figure 1B and 1C are relative to original paper (Mangold et al. [141]). (**b**) Mastcam-Z photograph of the hills of Kodiak. (**c**) Mastcam-Z image of the landing area delta. Panels (**d**–**g**) show different steep slopes in the landing area. Yellow arrows indicate the location of boulder-rich material. The black arrow indicates an exposure with dipping strata.

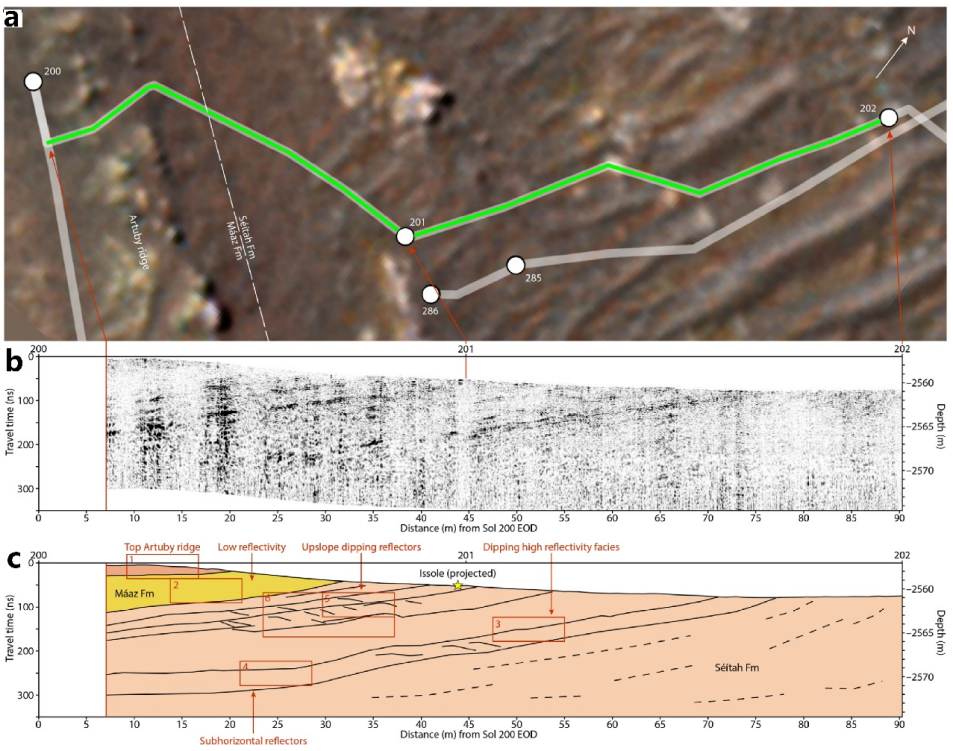

Figure 21. RIMFAX radar image of Perseverance and its geological interpretation (adapted from Hamran et al. [25]). (**a**) Route map of the Mars rover (green line) between sol 201 and 202. (**b**) RIMFAX radar observation image. (**c**) Geological interpretation.

The geological layering detected in the radargram is interpreted as igneous structures associated with the in situ laminated magma bodies (Hamran et al. [25]). At the highest resolution, there are multiple lenticular reflective surfaces with S-shaped profiles between the inclined high-reflectivity layers (Figure 21c), which are interpreted as magmatic flows and shear structures or as cyclic step structures. Radar images show the prevalence of strongly reflective sequences (intrusive strata), which are interpreted as sedimentary layers formed by igneous activity and multiple aqueous depositions, further validating the claim of a paleolake at Jezero Crater. However, the Perseverance radar currently does not find evidence of water ice at the landing zone. Nevertheless, it is anticipated that the rover, traveling longer distances, is expected to find evidence of water ice on the shallow surface layers of Mars (Hamran et al. [25]).

6. Prospect of In Situ Ground-Penetrating Radar on Mars: Detection of Water Ice

The main parameters of the ground-penetrating radar (GPR) radargram for distinguishing subsurface materials are relative permittivity and dielectric loss. The permittivity is complex, where the real part represents the relative permittivity and can be estimated by calculating the propagation velocity of the radar electromagnetic waves in the subsurface materials. The imaginary part represents the loss of electromagnetic waves in the medium, and the dielectric loss tangent is the ratio of the imaginary part to the real part of the complex permittivity. By calculating the values of the relative permittivity and the dielectric loss tangent from the radar echoes, it is possible to infer the subsurface structure and composition on Mars and potentially obtain evidence of the presence of water ice. However, when detecting water ice with radar, it is not possible to determine the uniqueness of the detected substance solely based on the relative permittivity and the dielectric loss of the medium. For instance, water ice typically exhibits a relative permittivity of $\sim$3, with a dielectric loss of less than 10^{-3} (Grima et al. [124], Orosei et al. [143], Nerozzi and Holt [144]), while low-density porous materials (e.g., Martian soil or volcanic ash) have similar those of values to water ice (Watters et al. [135], Carter et al. [136]). Therefore, it is insufficient to determine whether the detected material is water ice or low-density material based solely on these two parameters. It is necessary to approach the identification of water ice from multiple perspectives. This paper suggests several approaches to determine whether subsurface water ice is observed by the ground-penetrating radar:

1. Calculating the relative permittivity and the dielectric loss of the subsurface material based on the radar observations. If the calculated relative permittivity is greater than 4 and the value of the dielectric loss tangent is higher than 10^{-2}, it can be concluded that the detected region almost certainly does not contain water ice but possibly consists of volcanic basalt or other dense deposits.
2. Observing the echo features of the GPR radargram. Typically, water ice has an isotropic composition, which should result in fewer interior echoes and clean echoes with distinct interfaces between the water ice and the underlying layer in the radargram. However, Martian soil is primarily formed by impact cratering and space weathering, and its internal uniformity depends on the duration of weathering. It inevitably contains fragmented rocks internally, which can cause multiple reflections within the radar echoes.
3. Using multi-frequency radar observations. Laboratory studies have shown that the electromagnetic attenuation characteristics differ for different frequencies in basalt sand, pure water ice, and mixtures of water ice with different ratios (Mattei et al. [145]). The attenuation coefficient of electromagnetic waves in basalt sand is directly proportional to frequency, while the attenuation coefficient of water ice is independent of frequency.

In 2013, the Chinese Chang'e-3 mission carried the Moon-based GPR observing the geological stratigraphy of the Mare Imbrium on the nearside of the Moon (Fang et al. [48]). The subsequent Chang'e-4 and Chang'e-5 missions also carried the GPR instruments (Xiao et al. [49], Ding et al. [146,147], Su et al. [148]). Detailed parameters can be found

in Table 1. Currently, two deployed GPRs are operating on Mars: the RoPeR radar on the Zhurong rover (Zhou et al. [15]) and the RIMFAX radar on the Perseverance rover (Hamran et al. [14]). Table 1 contains the detailed parameters of those two radars. The RoPeR radar consists of a high-frequency channel and a low-frequency channel (Zhou et al. [15], Chen et al. [16], Li et al. [26]). The low-frequency channel's center frequency is 55 MHz, with a depth resolution of meters, theoretically capable of penetrating several tens of meters beneath the Martian surface (Zhou et al. [15], Li et al. [26]). The high-frequency channel operates at a center frequency of 1.30 GHz, with a depth resolution in the centimeter, capable of penetrating several meters below the Martian surface (Zhou et al. [15], Chen et al. [16]). RIMFAX has only one channel with a center frequency of 675 MHz and a depth resolution of 10–40 cm, capable of penetrating depths greater than 10 m beneath the Martian surface (Hamran et al. [14]). Additionally, the future ExoMars mission will also carry the WISDOM radar to detect the Martian surface. The center frequency of this radar is 1.75 GHz, with a depth resolution of ∼3 cm, capable of penetrating several meters beneath the Martian surface (Ciarletti et al. [47]). It is foreseeable that GPRs will play an important role in current and future surface exploration missions on Mars. This provides opportunities for the detection of subsurface water ice but also poses challenges in distinguishing low-density materials and water ice. Currently, none of the deployed Martian-based GPRs have more than two channels (Table 1). Therefore, to effectively detect shallow subsurface water ice on Mars, our paper suggests that future Martian surface exploration missions can consider GPR systems with more than two frequency channels. Analyzing the radar electromagnetic wave attenuation at different frequencies will be a key breakthrough in proving the presence of water ice detected by the in situ GPR.

7. Conclusions and Perspectives

Detecting water ice on Mars has been a crucial aspect of the Mars exploration project as it directly influences the planet's habitability and the potential for extraterrestrial life. The current approach to detecting Mars water ice is becoming more diverse, incorporating remote sensing photography, radar, measurements by gamma ray spectroscopy and neutron spectrometers, soil analysis, and the recent SWIM mapping project, which is a collaborative effort involving multiple devices. This expansion of detection methods is expected to provide more compelling evidence of Martian water ice soon.

The existence that there could have been liquid water on Mars in the past is becoming an increasingly robust argument, supported by the study of features such as the network of canyons, ancient lakes, oceanic remains, and the presence of hydrated minerals at various locations. Regarding the present presence of water ice on Mars, the widespread detection of hydrogen by spectroscopy suggests the possible abundance of water on the planet. Additionally, recurring slope lines (RSL) that have been observed in recent years are evidence of the current flow of liquid water on the Martian surface. Furthermore, bodies of liquid water have been observed below the ice caps in Mars' polar regions, making it one of the current research hotspots for Mars radar observations (Lauro et al. [113], Orosei et al. [149], Diez [150]).

Currently, Mars exploration primarily targets areas with remnants of paleolakes or oceans. These regions are ideal for investigating the geological evolution of Mars and the distribution of water ice. For instance, the Chryse Planitia, Utopia Plain, and Isidis Plain have numerous clues to the presence of subsurface water ice. The implementation of the SWIM mapping project has also revealed that future Mars radar exploration will likely rely on subsurface radar-based and multi-equipment collaboration.

The Jezero crater, where the Perseverance rover has recently landed, contains alluvial fans indicating paleolakes and strata formed by aqueous deposition. Although the short time available to Perseverance has prevented it from finding evidence of current water ice presence, the area remains ideal for exploring the geological evolution of Mars and the distribution of water ice hidden below the surface. Although Martian-based ground-penetrating radar is set to be deployed on the surface of Mars in 2020, ground-

penetrating radar technology was previously deployed on the nearside of the Moon in 2013 (Xiao et al. [151], Ding et al. [152]). Researchers can adapt from the experience gained through the Moon-based ground-penetrating radar for data processing (Ding et al. [152], Su et al. [153]), the inversion of the subsurface medium's dielectric property parameters (Feng et al. [154], Ding et al. [155], Li et al. [156]), and the construction of numerical models for the subsurface layers of Mars (Ding et al. [157,158]). We believe that with long-term and continuous observation of the Perseverance rover's ground-penetrating radar, as well as advanced data-processing methods and modeling simulations, it is possible to detect the existence of subsurface water ice or liquid water on Mars.

Author Contributions: Conceptualization, C.D.; methodology, N.Z., C.D. and R.O.; software, N.Z., C.D. and R.O.; validation, N.Z., C.D. and R.O.; formal analysis, N.Z., C.D. and Y.S.; investigation, N.Z., C.D. and R.O. resources, C.D., Y.S. and R.O.; data curation, N.Z. and C.D.; writing—original draft preparation, N.Z. and C.D.; writing—review and editing, C.D., Y.S. and R.O.; visualization, C.D.; project administration, C.D., Y.S. and R.O.; supervision, C.D. and R.O. funding acquisition, C.D. All authors have read and agreed to the published version of the manuscript.

Funding: This work is supported by the National Natural Science Foundation of China with Grant No. 42241139, 62227901 and 42004099, the Opening Fund of the Key Laboratory of Lunar and Deep Space Exploration, Chinese Academy of Sciences (No. LDSE202005), the National Innovation and Entrepreneurship Training Program for College Students (No. 202310590016), and Shenzhen Municipal Government Investment Project (No. 2106-440300-04-03-901272).

Acknowledgments: This work has been supported by the team "Searching for Subglacial Water on Mars with Orbiting Ground Penetrating Radars" of the International Space Science Institute (ISSI).

Conflicts of Interest: The authors declare no conflicts of interest.

References

1. Masursky, H. On Mars: Exploration of the Red Planet. *Eos Trans. Am. Geophys. Union* **1985**, *66*, 642–643. [CrossRef]
2. Zheng, Y.C. Mars exploration in 2020. *Innovation* **2020**, *1*, 100036. [CrossRef] [PubMed]
3. Li, C.; Zhang, R.; Yu, D.; Dong, G.; Liu, J.; Geng, Y.; Sun, Z.; Yan, W.; Ren, X.; Su, Y.; et al. China's Mars exploration mission and science investigation. *Space Sci. Rev.* **2021**, *217*, 57. [CrossRef]
4. Boynton, W.; Feldman, W.; Squyres, S.; Prettyman, T.; Bruckner, J.; Evans, L.; Reedy, R.; Starr, R.; Arnold, J.; Drake, D.; et al. Distribution of hydrogen in the near surface of Mars: Evidence for subsurface ice deposits. *Science* **2002**, *297*, 81–85. [CrossRef]
5. McDougal, M.S.; Lasswell, H.D.; Vlasic, I.A.; Smith, J.C. Enjoyment and Aquisition of Resources in Outer Space. *Penn Law Leg. Scholarsh. Repos.* **1962**, *111*, 521.
6. Kieffer, H.H. Mars south polar spring and summer temperatures: A residual CO_2 frost. *J. Geophys. Res.* **1979**, *84*, 8263–8288. [CrossRef]
7. Byrne, S.; Ingersoll, A.P. A sublimation model for Martian south polar ice features. *Science* **2003**, *299*, 1051–1053. [CrossRef]
8. Bibring, J.P.; Langevin, Y.; Poulet, F.; Gendrin, A.; Gondet, B.; Berthé, M.; Soufflot, A.; Drossart, P.; Combes, M.; Bellucci, G.; et al. Perennial water ice identified in the south polar cap of Mars. *Nature* **2004**, *428*, 627–630. [CrossRef]
9. Rennó, N.O.; Bos, B.J.; Catling, D.; Clark, B.C.; Drube, L.; Fisher, D.; Goetz, W.; Hviid, S.F.; Keller, H.U.; Kok, J.F.; et al. Possible physical and thermodynamical evidence for liquid water at the Phoenix landing site. *J. Geophys. Res. Planets* **2009**, *114*, E00E03. [CrossRef]
10. Clifford, S.M.; Parker, T.J. The evolution of the Martian hydrosphere: Implications for the fate of a primordial ocean and the current state of the northern plains. *Icarus* **2001**, *154*, 40–79. [CrossRef]
11. McEwen, A.S.; Hansen, C.; Delamere, W.A.; Eliason, E.; Herkenhoff, K.E.; Keszthelyi, L.; Gulick, V.; Kirk, R.L.; Mellon, M.; Grant, J.A.; et al. A closer look at water-related geologic activity on Mars. *Science* **2007**, *317*, 1706–1709. [CrossRef]
12. Michalski, J.R.; Goudge, T.A.; Crowe, S.A.; Cuadros, J.; Mustard, J.F.; Johnson, S.S. Geological diversity and microbiological potential of lakes on Mars. *Nat. Astron.* **2022**, *6*, 1133–1141. [CrossRef]
13. McEwen, A.S.; Dundas, C.M.; Mattson, S.S.; Toigo, A.D.; Ojha, L.; Wray, J.J.; Chojnacki, M.; Byrne, S.; Murchie, S.L.; Thomas, N. Recurring slope lineae in equatorial regions of Mars. *Nat. Geosci.* **2014**, *7*, 53–58. [CrossRef]
14. Hamran, S.E.; Paige, D.A.; Amundsen, H.E.; Berger, T.; Brovoll, S.; Carter, L.; Damsgård, L.; Dypvik, H.; Eide, J.; Eide, S.; et al. Radar imager for Mars' subsurface experiment—RIMFAX. *Space Sci. Rev.* **2020**, *216*, 1–39. [CrossRef]
15. Zhou, B.; Shen, S.; Lu, W.; Liu, Q.; Tang, C.; Li, S.; Fang, G. The Mars rover subsurface penetrating radar onboard China's Mars 2020 mission. *Earth Planet. Phys.* **2020**, *4*, 345–354. [CrossRef]
16. Chen, R.; Zhang, L.; Xu, Y.; Liu, R.; Bugiolacchi, R.; Zhang, X.; Chen, L.; Zeng, Z.; Liu, C. Martian soil as revealed by ground-penetrating radar at the Tianwen-1 landing site. *Geology* **2023**, *51*, 315–319. [CrossRef]

17. Zhang, L.; Li, C.; Zhang, J.; Zhou, B.; Zhao, Y.Y.S.; Liu, Y.; Di, K.; Mitchell, R.N.; Li, J.; Zhang, Z.; et al. Buried palaeo-polygonal terrain detected underneath Utopia Planitia on Mars by the Zhurong radar. *Nat. Astron.* **2024**, *8*, 69–76. [CrossRef]
18. Picardi, G.; Biccari, D.; Seu, R.; Plaut, J.; Johnson, W.; Jordan, R.; Safaeinili, A.; Gurnett, D.; Huff, R.; Orosei, R.; et al. MARSIS: Mars advanced radar for subsurface and ionosphere sounding. In *Mars Express: The Scientific Payload*; NASA/ADS: Cambridge, MA, USA, 2004; Volume 1240, pp. 51–69.
19. Picardi, G.; Plaut, J.J.; Biccari, D.; Bombaci, O.; Calabrese, D.; Cartacci, M.; Cicchetti, A.; Clifford, S.M.; Edenhofer, P.; Farrell, W.M.; et al. Radar soundings of the subsurface of Mars. *Science* **2005**, *310*, 1925–1928. [CrossRef]
20. Seu, R.; Biccari, D.; Orosei, R.; Lorenzoni, L.; Phillips, R.; Marinangeli, L.; Picardi, G.; Masdea, A.; Zampolini, E. SHARAD: The MRO 2005 shallow radar. *Planet. Space Sci.* **2004**, *52*, 157–166. [CrossRef]
21. Seu, R.; Phillips, R.J.; Biccari, D.; Orosei, R.; Masdea, A.; Picardi, G.; Safaeinili, A.; Campbell, B.A.; Plaut, J.J.; Marinangeli, L.; et al. SHARAD sounding radar on the Mars Reconnaissance Orbiter. *J. Geophys. Res. Planets* **2007**, *112*, E05S05. [CrossRef]
22. Hong, T.; Su, Y.; Fan, M.; Dai, S.; Lv, P.; Ding, C.; Zhang, Z.; Wang, R.; Liu, C.; Du, W.; et al. Flight Experiment Validation of Altitude Measurement Performance of MOSIR on Tianwen-1 Orbiter. *Remote Sens.* **2021**, *13*, 5049. [CrossRef]
23. Hong, T.; Su, Y.; Dai, S.; Zhang, Z.; Du, W.; Liu, C.; Liu, S.; Wang, R.; Ding, C.; Li, C. An Improved Method of Surface Clutter Simulation Based on Orbiting Radar in Tianwen-1 Mars Exploration. *Radio Sci.* **2022**, *57*, e2022RS007491. [CrossRef]
24. Qiu, X.; Ding, C. Radar Observation of the Lava Tubes on the Moon and Mars. *Remote Sens.* **2023**, *15*, 2850. [CrossRef]
25. Hamran, S.E.; Paige, D.A.; Allwood, A.; Amundsen, H.E.; Berger, T.; Brovoll, S.; Carter, L.; Casademont, T.M.; Damsgård, L.; Dypvik, H.; et al. Ground penetrating radar observations of subsurface structures in the floor of Jezero crater, Mars. *Sci. Adv.* **2022**, *8*, eabp8564. [CrossRef] [PubMed]
26. Li, C.; Zheng, Y.; Wang, X.; Zhang, J.; Wang, Y.; Chen, L.; Zhang, L.; Zhao, P.; Liu, Y.; Lv, W.; et al. Layered subsurface in Utopia Basin of Mars revealed by Zhurong rover radar. *Nature* **2022**, *610*, 308–312. [CrossRef] [PubMed]
27. Casademont, T.; Eide, S.; Shoemaker, E.; Liu, Y.; Nunes, D.; Russell, P.; Dypvik, H.; Amundsen, H.; Berger, T.; Hamran, S.E. RIMFAX Ground Penetrating Radar Reveals Dielectric Permittivity and Rock Density of Shallow Martian Subsurface. *J. Geophys. Res. Planets* **2023**, *128*, e2022JE007598. [CrossRef]
28. Herve, Y.; Ciarletti, V.; Le Gall, A.; Corbel, C.; Hassen-Khodja, R.; Benedix, W.; Plettemeier, D.; Humeau, O.; Vieau, A.J.; Lustrement, B.; et al. The WISDOM radar on board the ExoMars 2022 Rover: Characterization and calibration of the flight model. *Planet. Space Sci.* **2020**, *189*, 104939. [CrossRef]
29. Malin, M.; Danielson, G.; Ravine, M.; Soulanille, T. Design and development of the Mars Observer Camera. *Int. J. Imaging Syst. Technol.* **1991**, *3*, 76–91. [CrossRef]
30. Wiens, R.C.; Maurice, S.; Robinson, S.H.; Nelson, A.E.; Cais, P.; Bernardi, P.; Newell, R.T.; Clegg, S.; Sharma, S.K.; Storms, S.; et al. The SuperCam Instrument Suite on the NASA Mars 2020 Rover: Body Unit and Combined System Tests. *Space Sci. Rev.* **2020**, *217*, 4. [CrossRef] [PubMed]
31. Thomas, N.; Cremonese, G.; Ziethe, R.; Gerber, M.; Brändli, M.; Bruno, G.; Erismann, M.; Gambicorti, L.; Gerber, T.; Ghose, K.; et al. The Colour and Stereo Surface Imaging System (CaSSIS) for the ExoMars Trace Gas Orbiter. *Space Sci. Rev.* **2017**, *212*, 1897–1944. [CrossRef]
32. Martínez-Alonso, S.; Mellon, M.T.; Banks, M.E.; Keszthelyi, L.P.; McEwen, A.S.; Team, T.H. Evidence of volcanic and glacial activity in Chryse and Acidalia Planitiae, Mars. *Icarus* **2011**, *212*, 597–621. [CrossRef]
33. Pedersen, G.; Head, J., III; Wilson, L. Formation, erosion and exposure of Early Amazonian dikes, dike swarms and possible subglacial eruptions in the Elysium Rise/Utopia Basin Region, Mars. *Earth Planet. Sci. Lett.* **2010**, *294*, 424–439. [CrossRef]
34. Howari, F.M.; Sharma, M.; Xavier, C.M.; Nazzal, Y.; Alaydaroos, F. Atmospheric, Geomorphological, and Compositional Analysis of Martian Asimov and Hale Craters: Implications for Recurring Slope Lineae. *Front. Astron. Space Sci.* **2022**, *8*, 244. [CrossRef]
35. Pedersen, G.B.M.; Head, J.W. Evidence of widespread degraded Amazonian-aged ice-rich deposits in the transition between Elysium Rise and Utopia Planitia, Mars: Guidelines for the recognition of degraded ice-rich materials. *Planet. Space Sci.* **2010**, *58*, 1953–1970. [CrossRef]
36. Zhou, H.; Feng, X.; Zhou, B.; Dong, Z.; Fang, G.; Zeng, Z.; Liu, C.; Li, Y.; Lu, W. Polarized Orientation Calibration and Processing Strategies for Tianwen-1 Full-Polarimetric Mars Rover Penetrating Radar Data. *IEEE Trans. Geosci. Remote Sens.* **2022**, *60*, 5119914. [CrossRef]
37. Dong, Z.; Feng, X.; Zhou, H.; Liu, C.; Lu, Q.; Liang, W. Assessing the effects of induced field rotation on water ice detection of Tianwen-1 full-polarimetric Mars rover penetrating radar. *IEEE Trans. Geosci. Remote Sens.* **2021**, *60*, 1–13. [CrossRef]
38. Liu, H.; Li, J.; Meng, X.; Zhou, B.; Fang, G.; Spencer, B.F. Discrimination Between Dry and Water Ices by Full Polarimetric Radar: Implications for China's First Martian Exploration. *IEEE Trans. Geosci. Remote Sens.* **2022**, *61*, 5100111. [CrossRef]
39. Grima, C.; Kofman, W.; Herique, A.; Orosei, R.; Seu, R. Quantitative analysis of Mars surface radar reflectivity at 20 MHz. *Icarus* **2012**, *220*, 84–99. [CrossRef]
40. Nouvel, J.F.; Herique, A.; Kofman, W.; Safaeinili, A. Radar signal simulation: Surface modeling with the facet method. *Radio Sci.* **2004**, *39*, RS1013. [CrossRef]
41. Jordan, R.; Picardi, G.; Plaut, J.; Wheeler, K.; Kirchner, D.; Safaeinili, A.; Johnson, W.; Seu, R.; Calabrese, D.; Zampolini, E.; et al. The Mars express MARSIS sounder instrument. *Planet. Space Sci.* **2009**, *57*, 1975–1986. [CrossRef]
42. Xiong, S.; Muller, J.P.; Tao, Y.; Ding, C.; Zhang, B.; Li, Q. Combination of MRO SHARAD and deep-learning-based DTM to search for subsurface features in Oxia Planum, Mars. *Astron. Astrophys.* **2023**, *676*, A16. [CrossRef]

43. Bramson, A.M.; Byrne, S.; Putzig, N.E.; Sutton, S.; Plaut, J.J.; Brothers, T.C.; Holt, J.W. Widespread excess ice in arcadia planitia, Mars. *Geophys. Res. Lett.* **2015**, *42*, 6566–6574. [CrossRef]
44. Orosei, R.; Lauro, S.E.; Pettinelli, E.; Cicchetti, A.; Coradini, M.; Cosciotti, B.; Di Paolo, F.; Flamini, E.; Mattei, E.; Pajola, M.; et al. Radar evidence of subglacial liquid water on Mars. *Science* **2018**, *361*, 490–493. [CrossRef]
45. Fan, M.; Lyu, P.; Su, Y.; Du, K.; Zhang, Q.; Zhang, Z.; Dai, S.; Hong, T. The Mars orbiter subsurface investigation radar (MOSIR) on China's Tianwen-1 mission. *Space Sci. Rev.* **2021**, *217*, 8. [CrossRef]
46. Farley, K.A.; Williford, K.H.; Stack, K.M.; Bhartia, R.; Chen, A.; de la Torre, M.; Hand, K.; Goreva, Y.; Herd, C.D.; Hueso, R.; et al. Mars 2020 mission overview. *Space Sci. Rev.* **2020**, *216*, 1–41. [CrossRef]
47. Ciarletti, V.; Clifford, S.; Plettemeier, D.; Le Gall, A.; Hervé, Y.; Dorizon, S.; Quantin-Nataf, C.; Benedix, W.S.; Schwenzer, S.; Pettinelli, E. The WISDOM radar: Unveiling the subsurface beneath the ExoMars Rover and identifying the best locations for drilling. *Astrobiology* **2017**, *17*, 565–584. [CrossRef]
48. Fang, G.Y.; Zhou, B.; Ji, Y.C.; Zhang, Q.Y.; Shen, S.X.; Li, Y.X.; Guan, H.F.; Tang, C.J.; Gao, Y.Z.; Lu, W. Lunar Penetrating Radar onboard the Chang'e-3 mission. *Res. Astron. Astrophys.* **2014**, *14*, 1607. [CrossRef]
49. Xiao, Y.; Su, Y.; Dai, S.; Feng, J.; Xing, S.; Ding, C.; Li, C. Ground experiments of Chang'e-5 lunar regolith penetrating radar. *Adv. Space Res.* **2019**, *63*, 3404–3419. [CrossRef]
50. Evans, L.G.; Reedy, R.C.; Starr, R.D.; Kerry, K.E.; Boynton, W.V. Analysis of gamma ray spectra measured by Mars Odyssey. *J. Geophys. Res. Planets* **2006**, *111*, E03S04. [CrossRef]
51. Saunders, R.; Arvidson, R.; Badhwar, G.; Boynton, W.; Christensen, P.; Cucinotta, F.; Feldman, W.; Gibbs, R.; Kloss, C.; Landano, M.; et al. 2001 Mars Odyssey mission summary. *Space Sci. Rev.* **2004**, *110*, 1–36. [CrossRef]
52. Mitrofanov, I.; Anfimov, D.; Kozyrev, A.; Litvak, M.; Sanin, A.; Tret'Yakov, V.; Krylov, A.; Shvetsov, V.; Boynton, W.V.; Shinohara, C.; et al. Maps of subsurface hydrogen from the high energy neutron detector, Mars Odyssey. *Science* **2002**, *297*, 78–81. [CrossRef]
53. Mitrofanov, I.; Malakhov, A.; Bakhtin, B.; Golovin, D.; Kozyrev, A.; Litvak, M.; Mokrousov, M.; Sanin, A.; Tretyakov, V.; Vostrukhin, A.; et al. Fine Resolution Epithermal Neutron Detector (FREND) Onboard the ExoMars Trace Gas Orbiter. *Space Sci. Rev.* **2018**, *214*, 86. [CrossRef]
54. Mitrofanov, I.; Malakhov, A.; Djachkova, M.; Golovin, D.; Litvak, M.; Mokrousov, M.; Sanin, A.; Svedhem, H.; Zelenyi, L. The evidence for unusually high hydrogen abundances in the central part of Valles Marineris on Mars. *Icarus* **2022**, *374*, 114805. [CrossRef]
55. Nikiforov, S.; Mitrofanov, I.; Litvak, M.; Lisov, D.; Djachkova, M.; Jun, I.; Tate, C.; Sanin, A. Assessment of water content in martian subsurface along the traverse of the Curiosity rover based on passive measurements of the DAN instrument. *Icarus* **2020**, *346*, 113818. [CrossRef]
56. Mitrofanov, I.G.; Litvak, M.L.; Varenikov, A.B.; Barmakov, Y.N.; Behar, A.; Bobrovnitsky, Y.I.; Bogolubov, E.P.; Boynton, W.V.; Harshman, K.; Kan, E.; et al. Dynamic Albedo of Neutrons (DAN) Experiment Onboard NASA's Mars Science Laboratory. *Space Sci. Rev.* **2012**, *170*, 559–582. [CrossRef]
57. Busch, M.W.; Aharonson, O. Measuring subsurface water distribution using the Dynamic Albedo of Neutrons instrument on Mars Science Laboratory. *Nucl. Instrum. Methods Phys. Res. Sect. A Accel. Spectrometers Detect. Assoc. Equip.* **2008**, *592*, 393–399. [CrossRef]
58. Smith, P.; Tamppari, L.; Arvidson, R.; Bass, D.; Blaney, D.; Boynton, W.; Carswell, A.; Catling, D.; Clark, B.; Duck, T.; et al. Introduction to special section on the phoenix mission: Landing site characterization experiments, mission overviews, and expected science. *J. Geophys. Res. Planets* **2008**, *113*, E00A18. [CrossRef]
59. Bibring, J.P.; Langevin, Y.; Gendrin, A.; Gondet, B.; Poulet, F.; Berthé, M.; Soufflot, A.; Arvidson, R.; Mangold, N.; Mustard, J.; et al. Mars surface diversity as revealed by the OMEGA/Mars Express observations. *Science* **2005**, *307*, 1576–1581. [CrossRef] [PubMed]
60. Nazari-Sharabian, M.; Aghababaei, M.; Karakouzian, M.; Karami, M. Water on Mars—A literature review. *Galaxies* **2020**, *8*, 40. [CrossRef]
61. Stillman, D.E.; Michaels, T.I.; Grimm, R.E. Characteristics of the numerous and widespread recurring slope lineae (RSL) in Valles Marineris, Mars. *Icarus* **2017**, *285*, 195–210. [CrossRef]
62. Ojha, L.; Wilhelm, M.B.; Murchie, S.L.; McEwen, A.S.; Wray, J.J.; Hanley, J.; Massé, M.; Chojnacki, M. Spectral evidence for hydrated salts in recurring slope lineae on Mars. *Nat. Geosci.* **2015**, *8*, 829–832. [CrossRef]
63. Carter, J.; Poulet, F.; Bibring, J.P.; Mangold, N.; Murchie, S. Hydrous minerals on Mars as seen by the CRISM and OMEGA imaging spectrometers: Updated global view. *J. Geophys. Res. Planets* **2013**, *118*, 831–858. [CrossRef]
64. Sun, V.Z.; Milliken, R.E. Ancient and recent clay formation on Mars as revealed from a global survey of hydrous minerals in crater central peaks. *J. Geophys. Res. Planets* **2015**, *120*, 2293–2332. [CrossRef]
65. Wernicke, L.J.; Jakosky, B.M. Martian hydrated minerals: A significant water sink. *J. Geophys. Res. Planets* **2021**, *126*, e2019JE006351. [CrossRef]
66. Ehlmann, B.L.; Edwards, C.S. Mineralogy of the Martian surface. *Annu. Rev. Earth Planet. Sci.* **2014**, *42*, 291–315. [CrossRef]
67. Yen, A.S.; Gellert, R.; Schröder, C.; Morris, R.V.; Bell, J.F., III; Knudson, A.T.; Clark, B.C.; Ming, D.W.; Crisp, J.A.; Arvidson, R.E.; et al. An integrated view of the chemistry and mineralogy of Martian soils. *Nature* **2005**, *436*, 49–54. [CrossRef] [PubMed]

68. Chevrier, V.; Mathé, P.E. Mineralogy and evolution of the surface of Mars: A review. *Planet. Space Sci.* **2007**, *55*, 289–314. [CrossRef]
69. Craddock, R.A.; Howard, A.D. The case for rainfall on a warm, wet early Mars. *J. Geophys. Res. Planets* **2002**, *107*, 21-1–21-36. [CrossRef]
70. Carr, M.H.; Chuang, F.C. Martian drainage densities. *J. Geophys. Res. Planets* **1997**, *102*, 9145–9152. [CrossRef]
71. Hynek, B.M.; Beach, M.; Hoke, M.R. Updated global map of Martian valley networks and implications for climate and hydrologic processes. *J. Geophys. Res. Planets* **2010**, *115*, E09008. [CrossRef]
72. Fassett, C.I.; Head, J.W., III. The timing of Martian valley network activity: Constraints from buffered crater counting. *Icarus* **2008**, *195*, 61–89. [CrossRef]
73. Di Achille, G.; Hynek, B.M. Ancient ocean on Mars supported by global distribution of deltas and valleys. *Nat. Geosci.* **2010**, *3*, 459–463. [CrossRef]
74. Di Achille, G.; Hynek, B.M. Deltas and valley networks on Mars: Implications for a global hydrosphere. In *Lakes on Mars*; Elsevier Science: Amsterdam, The Netherlands, 2010; pp. 223–248.
75. Kamada, A.; Kuroda, T.; Kasaba, Y.; Terada, N.; Nakagawa, H. Global climate and river transport simulations of early Mars around the Noachian and Hesperian boundary. *Icarus* **2021**, *368*, 114618. [CrossRef]
76. Golombek, M.; Grant, J.A.; Parker, T.; Kass, D.; Crisp, J.; Squyres, S.W.; Haldemann, A.; Adler, M.; Lee, W.; Bridges, N.; et al. Selection of the Mars Exploration Rover landing sites. *J. Geophys. Res. Planets* **2003**, *108*, 8072. [CrossRef]
77. Grotzinger, J.P.; Crisp, J.A.; Vasavada, A.R.; Team, M.S. Curiosity's mission of exploration at Gale Crater, Mars. *Elements* **2015**, *11*, 19–26. [CrossRef]
78. Goudge, T.A.; Fassett, C.I.; Head, J.W.; Mustard, J.F.; Aureli, K.L. Insights into surface runoff on early Mars from paleolake basin morphology and stratigraphy. *Geology* **2016**, *44*, 419–422. [CrossRef]
79. Burr, D.; Jacobsen, R.; Lefort, A.; Borden, R.; Peel, S. Summary of Findings from a USGS Scientific Investigations Map (SIM) at 1:500 k of the Aeolis Dorsa Region, Mars. In Proceedings of the 52nd Lunar and Planetary Science Conference, virtual event, 15–19 March 2021; Number 2548, p. 1315.
80. Peel, S.; Burr, D. Lack of evidence for paleolakes in the Aeolis Dorsa region, Mars; A mapping investigation. *Planet. Space Sci.* **2022**, *216*, 105445. [CrossRef]
81. Mouginot, J.; Pommerol, A.; Beck, P.; Kofman, W.; Clifford, S.M. Dielectric map of the Martian northern hemisphere and the nature of plain filling materials. *Geophys. Res. Lett.* **2012**, *39*, L02202. [CrossRef]
82. Liu, C.; Ling, Z.; Wu, Z.; Zhang, J.; Chen, J.; Fu, X.; Qiao, L.; Liu, P.; Li, B.; Zhang, L.; et al. Aqueous alteration of the Vastitas Borealis Formation at the Tianwen-1 landing site. *Commun. Earth Environ.* **2022**, *3*, 280. [CrossRef]
83. Xiao, L.; Huang, J.; Kusky, T.; Head, J.; Zhao, J.; Wang, J.; Wang, L.; Yu, W.; Shi, Y.; Wu, B.; et al. Evidence for marine sedimentary rocks in Utopia Planitia: Zhurong rover observations. *Natl. Sci. Rev.* **2023**, *10*, nwad137. [CrossRef]
84. Carr, M.; Crumpler, L.; Cutts, J.; Greeley, R.; Guest, J.; Masursky, H. Martian impact craters and emplacement of ejecta by surface flow. *J. Geophys. Res.* **1977**, *82*, 4055–4065. [CrossRef]
85. Osinski, G.R. Effect of volatiles and target lithology on the generation and emplacement of impact crater fill and ejecta deposits on Mars. *Meteorit. Planet. Sci.* **2006**, *41*, 1571–1586. [CrossRef]
86. Mantegazza, M.; Spagnuolo, M.G.; Rossi, A.P. Multidisciplinary analysis of pit craters at Hale Crater, Mars. *Icarus* **2023**, *397*, 115495. [CrossRef]
87. McCauley, J.F. Mariner 9 evidence for wind erosion in the equatorial and mid-latitude regions of Mars. *J. Geophys. Res.* **1973**, *78*, 4123–4137. [CrossRef]
88. Wulf, G.; Hergarten, S.; Kenkmann, T. Combined remote sensing analyses and landform evolution modeling reveal the terrestrial Bosumtwi impact structure as a Mars-like rampart crater. *Earth Planet. Sci. Lett.* **2019**, *506*, 209–220. [CrossRef]
89. Carr, M.H.; Masursky, H.; Baum, W.A.; Blasius, K.R.; Briggs, G.A.; Cutts, J.A.; Duxbury, T.; Greeley, R.; Guest, J.E.; Smith, B.A. Preliminary results from the Viking orbiter imaging experiment. *Science* **1976**, *193*, 766–776. [CrossRef]
90. Stewart, S.; O'Keefe, J.; Ahrens, T. The relationship between rampart crater morphologies and the amount of subsurface ice. In Proceedings of the 32nd Lunar and Planetary Science Conference, Houston, TX, USA, 12–16 March 2001; p. 2092.
91. Scott, D.H.; Tanaka, K.L. *Geologic Map of the Western Equatorial Region of Mars*; Citeseer: Forest Grove, OR, USA, 1986; Volume 1.
92. Helfenstein, P.; Mouginis-Mark, P. Morphology and distribution of fractured terrain on Mars. In Proceedings of the Lunar and Planetary Science Conference, Houston, TX, USA, 17–21 March 1980; Volume 11, pp. 429–431.
93. Hiesinger, H.; Head, J.W., III. Characteristics and origin of polygonal terrain in southern Utopia Planitia, Mars: Results from Mars Orbiter Laser Altimeter and Mars Orbiter Camera data. *J. Geophys. Res. Planets* **2000**, *105*, 11999–12022. [CrossRef]
94. McGill, G.E.; Hills, L.S. Origin of giant Martian polygons. *J. Geophys. Res. Planets* **1992**, *97*, 2633–2647. [CrossRef]
95. Pechmann, J.C. The origin of polygonal troughs on the northern plains of Mars. *Icarus* **1980**, *42*, 185–210. [CrossRef]
96. Seibert, N.M.; Kargel, J.S. Small-scale Martian polygonal terrain: Implications for liquid surface water. *Geophys. Res. Lett.* **2001**, *28*, 899–902. [CrossRef]
97. Wenrich, M.; Christensen, P. A formational model for the Martian polygonal terrains. In Proceedings of the Lunar and Planetary Science Conference, Houston, TX, USA, 18–22 March 1996; Volume 27.
98. Mellon, M.T. Small-scale polygonal features on Mars: Seasonal thermal contraction cracks in permafrost. *J. Geophys. Res. Planets* **1997**, *102*, 25617–25628. [CrossRef]

99. Wang, J.; Zhao, J.; Xiao, L.; Peng, S.; Zhang, L.; Zhang, Z.; Gao, A.; Qiao, H.; Wang, L.; Zhang, S.; et al. Recent Aqueous Activity on Mars Evidenced by Transverse Aeolian Ridges in the Zhurong Exploration Region of Utopia Planitia. *Geophys. Res. Lett.* **2023**, *50*, e2022GL101650. [CrossRef]
100. Liu, J.; Li, C.; Zhang, R.; Rao, W.; Cui, X.; Geng, Y.; Jia, Y.; Huang, H.; Ren, X.; Yan, W.; et al. Geomorphic contexts and science focus of the Zhurong landing site on Mars. *Nat. Astron.* **2021**, *6*, 65–71. [CrossRef]
101. Hamilton, C.W.; Fagents, S.A.; Thordarson, T. Lava–ground ice interactions in Elysium Planitia, Mars: Geomorphological and geospatial analysis of the Tartarus Colles cone groups. *J. Geophys. Res. Planets* **2011**, *116*, E03004. [CrossRef]
102. Liu, Y.; Wu, X.; Zhao, Y.Y.S.; Pan, L.; Wang, C.; Liu, J.; Zhao, Z.; Zhou, X.; Zhang, C.; Wu, Y.; et al. Zhurong reveals recent aqueous activities in Utopia Planitia, Mars. *Sci. Adv.* **2022**, *8*, eabn8555. [CrossRef]
103. Zhao, Y.S.; Yu, J.; Wei, G.; Pan, L.; Liu, X.; Lin, Y.; Liu, Y.; Sun, C.; Wang, X.; Wang, J.; et al. In situ analysis of surface composition and meteorology at the Zhurong landing site on Mars. *Natl. Sci. Rev.* **2023**, *10*, nwad056. [CrossRef]
104. Qin, X.; Ren, X.; Wang, X.; Liu, J.; Wu, H.; Zeng, X.; Sun, Y.; Chen, Z.; Zhang, S.; Zhang, Y.; et al. Modern water at low latitudes on Mars: Potential evidence from dune surfaces. *Sci. Adv.* **2023**, *9*, eadd8868. [CrossRef] [PubMed]
105. Williams, J.M.; Scuderi, L.A.; Newsom, H.E. Numerical Analysis of Putative Rock Glaciers on Mount Sharp, Gale Crater, Mars. *Remote Sens.* **2022**, *14*, 1887. [CrossRef]
106. Mellon, M.T.; Jakosky, B.M. Geographic variations in the thermal and diffusive stability of ground ice on Mars. *J. Geophys. Res. Planets* **1993**, *98*, 3345–3364. [CrossRef]
107. Titus, T.N.; Kieffer, H.H.; Christensen, P.R. Exposed water ice discovered near the south pole of Mars. *Science* **2003**, *299*, 1048–1051. [CrossRef] [PubMed]
108. Gourronc, M.; Bourgeois, O.; Mmaoge, D.; Pochat, S.; Bultel, B.; Massmao, M.; Le Deit, L.; Le Moumaolic, S.; Mercier, D. One million cubic kilometers of fossil ice in Valles Marineris: Relicts of a 3.5 Gy old glacial landsystem along the Martian equator. *Geomorphology* **2014**, *204*, 235–255. [CrossRef]
109. Vijayan, S.; Mangold, N.; Bhardwaj, A. Water-Ice Exposing Scarps within the Northern Midlatitude Craters on Mars. *Geophys. Res. Lett.* **2020**, *47*, e2020GL089057.
110. Butcher, F.E.G. *Water Ice at Mid-Latitudes on Mars*; Oxford University Press: Oxford, UK, 2022. [CrossRef]
111. Vandaele, A.C.; Lopez-Moreno, J.J.; Patel, M.R.; Bellucci, G.; Daerden, F.; Ristic, B.; Robert, S.; Thomas, I.R.; Wilquet, V.; Allen, M.; et al. NOMAD, an Integrated Suite of Three Spectrometers for the ExoMars Trace Gas Mission: Technical Description, Science Objectives and Expected Performance. *Space Sci. Rev.* **2018**, *214*, 80. [CrossRef]
112. Murchie, S.; Arvidson, R.; Bedini, P.; Beisser, K.; Bibring, J.P.; Bishop, J.; Boldt, J.; Cavender, P.; Choo, T.; Clancy, R.T.; et al. Compact Reconnaissance Imaging Spectrometer for Mars (CRISM) on Mars Reconnaissance Orbiter (MRO). *J. Geophys. Res. Planets* **2007**, *112*, E05S03. [CrossRef]
113. Lauro, S.E.; Pettinelli, E.; Caprarelli, G.; Guallini, L.; Rossi, A.P.; Mattei, E.; Cosciotti, B.; Cicchetti, A.; Soldovieri, F.; Cartacci, M.; et al. Multiple subglacial water bodies below the south pole of Mars unveiled by new MARSIS data. *Nat. Astron.* **2021**, *5*, 63–70. [CrossRef]
114. Ojha, L.; Karimi, S.; Buffo, J.; Nerozzi, S.; Holt, J.W.; Smrekar, S.; Chevrier, V. Martian Mantle Heat Flow Estimate From the Lack of Lithospheric Flexure in the South Pole of Mars: Implications for Planetary Evolution and Basal Melting. *Geophys. Res. Lett.* **2021**, *48*, e2020GL091409. [CrossRef]
115. Bierson, C.J.; Tulaczyk, S.; Courville, S.W.; Putzig, N.E. Strong MARSIS Radar Reflections from the Base of Martian South Polar Cap May Be Due to Conductive Ice or Minerals. *Geophys. Res. Lett.* **2021**, *48*, e2021GL093880. [CrossRef]
116. Smith, I.B.; Lalich, D.E.; Rezza, C.; Horgan, B.H.N.; Whitten, J.L.; Nerozzi, S.; Holt, J.W. A Solid Interpretation of Bright Radar Reflectors under the Mars South Polar Ice. *Geophys. Res. Lett.* **2021**, *48*, e2021GL093618. [CrossRef]
117. Lalich, D.E.; Hayes, A.G.; Poggiali, V. Explaining Bright Radar Reflections Below The South Pole of Mars without Liquid Water. *Nat. Astron.* **2022**, *6*, 1142–1146. [CrossRef]
118. Grima, C.; Mouginot, J.; Kofman, W.; Hmaorique, A.; Beck, P. The Basal Detectability of an Ice-Covered Mars by MARSIS. *Geophys. Res. Lett.* **2022**, *49*, e2021GL096518. [CrossRef]
119. Mattei, E.; Pettinelli, E.; Lauro, S.E.; Stillman, D.E.; Cosciotti, B.; Marinangeli, L.; Tangari, A.C.; Soldovieri, F.; Orosei, R.; Caprarelli, G. Assessing the role of clay and salts on the origin of MARSIS basal bright reflections. *Earth Planet. Sci. Lett.* **2022**, *579*, 117370. [CrossRef]
120. Cosciotti, B.; Mattei, E.; Brin, A.; Lauro, S.E.; Stillman, D.E.; Cunje, A.; Hickson, D.; Caprarelli, G.; Pettinelli, E. Can Clay Mimic the High Reflectivity of Briny Water Below the Martian SPLD? *J. Geophys. Res. Planets* **2023**, *128*, e2022JE007513. [CrossRef]
121. Bain, Z.; Morgan, G.; Putzig, N.; Campbell, B.; Bramson, A.; Petersen, E.; Mastrogiuseppe, M.; Perry, M.; Baker, D.H.; Smith, I.; et al. MARS Subsurface Water Ice Mapping (SWIM): Radar Surface Reflectivity. In Proceedings of the 50th Lunar and Planetary Science Conference, The Woodlands, TX, USA, 18–22 March 2019.
122. Morgan, G.A.; Putzig, N.E.; Perry, M.R.; Sizemore, H.G.; Bramson, A.M.; Petersen, E.I.; Bain, Z.M.; Baker, D.M.; Mastrogiuseppe, M.; Hoover, R.H.; et al. Availability of subsurface water-ice resources in the northern mid-latitudes of Mars. *Nat. Astron.* **2021**, *5*, 230–236. [CrossRef]
123. Farrell, W.; Plaut, J.; Gurnett, D.; Picardi, G. Detecting sub-glacial aquifers in the north polar layered deposits with Mars Express/MARSIS. *Geophys. Res. Lett.* **2005**, *32*. [CrossRef]

124. Grima, C.; Kofman, W.; Mouginot, J.; Phillips, R.J.; Hérique, A.; Biccari, D.; Seu, R.; Cutigni, M. North polar deposits of Mars: Extreme purity of the water ice. *Geophys. Res. Lett.* **2009**, *36*, L03203. [CrossRef]
125. Levrard, B.; Forget, F.; Montmessin, F.; Laskar, J. Recent ice-rich deposits formed at high latitudes on Mars by sublimation of unstable equatorial ice during low obliquity. *Nature* **2004**, *431*, 1072–1075. [CrossRef] [PubMed]
126. Zhou, J.; Ding, C.; Xiong, S.; Su, Y.; Li, J.; Chen, M.; Dai, S. Radar Observations of Liquid Water in the South Polar Region of Mars: Indications from Astrobiology Perspectives. *Universe* **2024**, *10*, 43. [CrossRef]
127. Garvin, J.B.; Soare, R.J.; Hepburn, A.J.; Koutnik, M.; Godin, E. Ice Exploration on Mars: Where to and when? In *Ices in the Solar-System*; Elsevier: Amsterdam, The Netherlands, 2024; pp. 193–219.
128. Putzig, N.E.; Morgan, G.A.; Sizemore, H.G.; Hollibaugh Baker, D.M.; Petersen, E.I.; Pathare, A.V.; Dundas, C.M.; Bramson, A.M.; Courville, S.W.; Perry, M.R.; et al. Ice resource mapping on Mars. In *Handbook of Space Resources*; Springer: New York, NY, USA, 2023; pp. 583–616.
129. Plaut, J.J.; Picardi, G.; Safaeinili, A.; Ivanov, A.B.; Milkovich, S.M.; Cicchetti, A.; Kofman, W.; Mouginot, J.; Farrell, W.M.; Phillips, R.J.; et al. Subsurface radar sounding of the south polar layered deposits of Mars. *Science* **2007**, *316*, 92–95. [CrossRef] [PubMed]
130. Phillips, R.J.; Zuber, M.T.; Smrekar, S.E.; Mellon, M.T.; Head, J.W.; Tanaka, K.L.; Putzig, N.E.; Milkovich, S.M.; Campbell, B.A.; Plaut, J.J.; et al. Mars north polar deposits: Stratigraphy, age, and geodynamical response. *Science* **2008**, *320*, 1182–1185. [CrossRef] [PubMed]
131. Putzig, N.E.; Seu, R.; Morgan, G.A.; Smith, I.B.; Campbell, B.A.; Perry, M.R.; Mastrogiuseppe, M.; the MRO SHARAD team. Science results from sixteen years of MRO SHARAD operations. *Icarus* **2023**, *2023*, 115715. [CrossRef]
132. Stuurman, C.; Osinski, G.; Holt, J.; Levy, J.; Brothers, T.; Kerrigan, M.; Campbell, B. SHARAD detection and characterization of subsurface water ice deposits in Utopia Planitia, Mars. *Geophys. Res. Lett.* **2016**, *43*, 9484–9491. [CrossRef]
133. Plaut, J.J.; Safaeinili, A.; Holt, J.W.; Phillips, R.J.; Head, J.W., III; Seu, R.; Putzig, N.E.; Frigeri, A. Radar evidence for ice in lobate debris aprons in the mid-northern latitudes of Mars. *Geophys. Res. Lett.* **2009**, *36*, L02203. [CrossRef]
134. Dundas, C.M.; Bramson, A.M.; Ojha, L.; Wray, J.J.; Mellon, M.T.; Byrne, S.; McEwen, A.S.; Putzig, N.E.; Viola, D.; Sutton, S.; et al. Exposed subsurface ice sheets in the Martian mid-latitudes. *Science* **2018**, *359*, 199–201. [CrossRef]
135. Watters, T.R.; Campbell, B.; Carter, L.; Leuschen, C.J.; Plaut, J.J.; Picardi, G.; Orosei, R.; Safaeinili, A.; Clifford, S.M.; Farrell, W.M.; et al. Radar sounding of the Medusae Fossae Formation Mars: Equatorial ice or dry, low-density deposits? *Science* **2007**, *318*, 1125–1128. [CrossRef]
136. Carter, L.M.; Campbell, B.A.; Watters, T.R.; Phillips, R.J.; Putzig, N.E.; Safaeinili, A.; Plaut, J.J.; Okubo, C.H.; Egan, A.F.; Seu, R.; et al. Shallow radar (SHARAD) sounding observations of the Medusae Fossae Formation, Mars. *Icarus* **2009**, *199*, 295–302. [CrossRef]
137. Campbell, B.A.; Watters, T.R.; Morgan, G.A. Dielectric properties of the medusae fossae formation and implications for ice content. *J. Geophys. Res. Planets* **2021**, *126*, e2020JE006601. [CrossRef]
138. Watters, T.R.; Campbell, B.A.; Leuschen, C.J.; Morgan, G.A.; Cicchetti, A.; Orosei, R.; Plaut, J.J. Evidence of Ice-Rich Layered Deposits in the Medusae Fossae Formation of Mars. *Geophys. Res. Lett.* **2024**, *51*, e2023GL105490. [CrossRef]
139. Goudge, T.A.; Mustard, J.F.; Head, J.W.; Fassett, C.I.; Wiseman, S.M. Assessing the mineralogy of the watershed and fan deposits of the Jezero crater paleolake system, Mars. *J. Geophys. Res. Planets* **2015**, *120*, 775–808. [CrossRef]
140. Fassett, C.I.; Head, J.W., III. Fluvial sedimentary deposits on Mars: Ancient deltas in a crater lake in the Nili Fossae region. *Geophys. Res. Lett.* **2005**, *32*. [CrossRef]
141. Mangold, N.; Gupta, S.; Gasnault, O.; Dromart, G.; Tarnas, J.; Sholes, S.; Horgan, B.; Quantin-Nataf, C.; Brown, A.; Le Mouélic, S.; et al. Perseverance rover reveals an ancient delta-lake system and flood deposits at Jezero crater, Mars. *Science* **2021**, *374*, 711–717. [CrossRef]
142. Bell, J.F., III; Maki, J.N.; Alwmark, S.; Ehlmann, B.L.; Fagents, S.A.; Grotzinger, J.P.; Gupta, S.; Hayes, A.; Herkenhoff, K.E.; Horgan, B.H.; et al. Geological, multispectral, and meteorological imaging results from the Mars 2020 Perseverance rover in Jezero crater. *Sci. Adv.* **2022**, *8*, eabo4856. [CrossRef]
143. Orosei, R.; Rossi, A.P.; Cantini, F.; Caprarelli, G.; Carter, L.M.; Papiano, I.; Cartacci, M.; Cicchetti, A.; Noschese, R. Radar sounding of Lucus Planum, Mars, by MARSIS. *J. Geophys. Res. Planets* **2017**, *122*, 1405–1418. [CrossRef]
144. Nerozzi, S.; Holt, J. Buried ice and sand caps at the north pole of Mars: Revealing a record of climate change in the cavi unit with SHARAD. *Geophys. Res. Lett.* **2019**, *46*, 7278–7286. [CrossRef]
145. Mattei, E.; Lauro, S.; Vannaroni, G.; Cosciotti, B.; Bella, F.; Pettinelli, E. Dielectric measurements and radar attenuation estimation of ice/basalt sand mixtures as martian Polar Caps analogues. *Icarus* **2014**, *229*, 428–433. [CrossRef]
146. Ding, C.; Xiao, Z.; Wu, B.; Li, Y.; Prieur, N.C.; Cai, Y.; Su, Y.; Cui, J. Fragments delivered by secondary craters at the Chang'E-4 landing site. *Geophys. Res. Lett.* **2020**, *47*, e2020GL087361. [CrossRef]
147. Ding, C.; Su, Y.; Lei, Z.; Zhang, Z.; Song, M.; Liu, Y.; Wang, R.; Li, Q.; Li, C.; Huang, S. Electromagnetic Signal Attenuation Characteristics in the Lunar Regolith Observed by the Lunar Regolith Penetrating Radar (LRPR) Onboard the Chang'E-5 Lander. *Remote Sens.* **2022**, *14*, 5189. [CrossRef]
148. Su, Y.; Wang, R.; Deng, X.; Zhang, Z.; Zhou, J.; Xiao, Z.; Ding, C.; Li, Y.; Dai, S.; Ren, X.; et al. Hyperfine structure of regolith unveiled by Chang'E-5 lunar regolith penetrating radar. *IEEE Trans. Geosci. Remote Sens.* **2022**, *60*, 1–14. [CrossRef]

149. Orosei, R.; Ding, C.; Fa, W.; Giannopoulos, A.; Hérique, A.; Kofman, W.; Lauro, S.E.; Li, C.; Pettinelli, E.; Su, Y.; et al. The global search for liquid water on Mars from orbit: Current and future perspectives. *Life* **2020**, *10*, 120. [CrossRef] [PubMed]
150. Diez, A. Liquid water on Mars. *Science* **2018**, *361*, 448–449. [CrossRef]
151. Xiao, L.; Zhu, P.; Fang, G.; Xiao, Z.; Zou, Y.; Zhao, J.; Zhao, N.; Yuan, Y.; Qiao, L.; Zhang, X.; et al. A young multilayered terrane of the northern Mare Imbrium revealed by Chang'E-3 mission. *Science* **2015**, *347*, 1226–1229. [CrossRef]
152. Ding, C.; Li, C.; Xiao, Z.; Su, Y.; Xing, S.; Wang, Y.; Feng, J.; Dai, S.; Xiao, Y.; Yao, M. Layering structures in the porous material beneath the Chang'e-3 landing site. *Earth Space Sci.* **2020**, *7*, e2019EA000862. [CrossRef]
153. Su, Y.; Xing, S.; Feng, J.; Dai, S.; Ding, C.; Xiao, Y.; Zhang, H.; Zhao, S.; Xue, X.; Zhang, X.; et al. Data Processing and Primary results of Lunar Penetrating Radar on Board the Chinese Yutu Rover. In Proceedings of the EGU General Assembly Conference Abstracts, Vienna, Austria, 12–17 April 2015; p. 4282.
154. Feng, J.; Su, Y.; Ding, C.; Xing, S.; Dai, S.; Zou, Y. Dielectric properties estimation of the lunar regolith at CE-3 landing site using lunar penetrating radar data. *Icarus* **2017**, *284*, 424–430. [CrossRef]
155. Ding, C.; Xiao, Z.; Su, Y.; Zhao, J.; Cui, J. Compositional variations along the route of Chang'e-3 Yutu rover revealed by the lunar penetrating radar. *Prog. Earth Planet. Sci.* **2020**, *7*, 1–11. [CrossRef]
156. Li, C.; Su, Y.; Pettinelli, E.; Xing, S.; Ding, C.; Liu, J.; Ren, X.; Lauro, S.E.; Soldovieri, F.; Zeng, X.; et al. The Moon's farside shallow subsurface structure unveiled by Chang'E-4 Lunar Penetrating Radar. *Sci. Adv.* **2020**, *6*, eaay6898. [CrossRef]
157. Ding, C.; Su, Y.; Xing, S.; Dai, S.; Xiao, Y.; Feng, J.; Liu, D.; Li, C. Numerical simulations of the lunar penetrating radar and investigations of the geological structures of the lunar regolith layer at the Chang'E 3 landing site. *Int. J. Antennas Propag.* **2017**, *2017*, 3013249. [CrossRef]
158. Ding, C.; Xiong, S.; Li, J.; Su, Y.; Huang, S. Yutu-2 radar observation of the lunar regolith heterogeneity at the Chang'E-4 landing site. *Astron. Astrophys.* **2022**, *664*, A43. [CrossRef]